공학박사학위논문

Simulation-based Framework to Improve Feasibility of Intensified Eco-friendly Chemical Processes

강화된 친환경 화학 공정의 타당성 개선을 위한 시뮬레이션 기반 연구

2021 년 8 월

서울대학교 대학원

화학생물공학부

이 동 우

Simulation-based Framework to Improve Feasibility of Intensified Eco-friendly Chemical Processes

지도교수 이 종 민

이 논문을 공학박사 학위논문으로 제출함

2021년 8월

서울대학교 대학원

화학생물공학부

이 동 우

이 동 우의 공학박사 학위논문을 인준함

2021년 8월

위 원 장 _____ 이 원 보 _____

부위원장 _____ 이 종 민 _____

위 원 _____ 남 재 욱 _____

위 원 _____ 나 종 걸 _____

위 원 _____ 정 동 휘 _____

Abstract

Simulation-based Framework to Improve Feasibility of Intensified Eco-friendly Chemical Processes

Dongwoo Lee

School of Chemical & Biological Engineering

The Graduate School of Seoul National University

Technologies to mitigate risks from climate change have made significant advances in both research academia and industry. However, most advanced techniques were still considered only in the lab-scale experience. Moreover, the process intensification development during the process synthesis is in its incipient stages. To promote the application of a novel process technique to an eco-friendly process, the process feasibility of economy or operation should be considered.

In this thesis, simulation-based framework to improve feasibility of intensified chemical processes, which are suggested under limited experimental conditions, is proposed. To solve the feasibility problem derived from the characteristics of process intensification, which is mainly developed by the numerous experiments rather than derived from the theoretical verification, the

digital twin technology, which is developed to simulate various situations by modeling the reactor and process, is implemented. In addition, the framework, including the procedures from verification or validation of developed digital twin model to feasibility study and improvement of economic and operational feasibility, is proposed.

First, intensified eco-friendly processes such as the biodiesel production process and carbon capture and utilization process were simulated, and comparative study and optimization were conducted to improve the economic or operational feasibility of that processes. As an example of applying the procedure to verify and to improve the economic feasibility, the economic feasibility study on the intensified biodiesel production process is implemented to increase the profitability of the biodiesel production process by reducing the process units, enhancing biodiesel quality, and reducing the raw material cost. As an example of applying the procedure to verify and to improve the operational feasibility, the modeling and validation of the semi-continuous carbonation process are implemented to estimate the overall CO_2 removal efficiency during the operation and when the reaction ends. Using the developed process model, the operational feasibility of the semi-continuous carbonation process is verified and the optimization algorithms is adopted to obtain the optimal operation recipes. For the effective operational feasibility improvement, two new operation recipes were suggested and optimized via Bayesian optimization.

Consequently, in order to verify and improve the applicability of the newly proposed intensified process, a methodology is proposed including the process

modeling, which is conducted using laboratory-scale experimental data for the reaction kinetic studies, economic analysis, sensitivity analysis, and comparative study. In addition, the process modeling and optimization, using pilot-scale operation data, are carried out. Especially, the operational feasibility of semi-continuous carbonation process is effectively improved by proposing new operation recipe as well as adopting the digital twin model to the Black-box optimization method.

In this thesis, a framework, improving economic/operational feasibility of newly proposed intensified chemical processes with two different experimental data depending on the purpose, is developed.

Keywords: Process intensification, Biodiesel production process, Carbon capture and utilization process, Black-box reactor model, Bayesian optimization.

Student Number: 2015-22820

Contents

List of Figures

List of Tables

Chapter 1

Introduction

1.1 Research motivation

Technologies to mitigate risks from climate change have made significant advances in both research academia and industry. The studies have focused on reducing carbon emissions as well as increasing the use of alternative energy sources, including solar, geothermal, hydrogen, and biomass. Developed techniques with the process integration approach, which minimizes raw material use and emissions through recycling and maximizes heat recovery to improve energy efficiency, and the process intensification approach, which combines multiple operations into fewer devices, have provided an extensive efficiency improvement to the eco-friendly processes. Although such efforts are being made the eco-friendly process to be successfully implemented at the industrial scale, there still remain challenges. First of all, most advanced techniques were still considered only in the lab-scale experience, for example, the experience with a novel catalyst, reactor or distillation column, and their combinations have been conducted to improve the process efficiency. Moreover, the process intensification development during the process synthesis is in its incipient stages. To promote the application of a novel process technique to an eco-friendly process, process feasibility such as economy and operation should be considered.

In this thesis, intensified eco-friendly processes such as the biodiesel production process and carbon capture and utilization process were simulated,

and comparative study and optimization were conducted to figure out the economic and operational feasibility of that processes, respectively. First, the biodiesel production process was simulated with a novel catalyst, and a comparative study was included to figure out the economic feasibility of the biodiesel production process with a Pd/Al_2O_3 catalyst. With Pd/Al_2O_3 catalyst, the supercritical transesterification and partial hydrogenation reactions occur simultaneously under milder reaction conditions than that of the conventional biodiesel production process. This combination of two reactions under the existence of the catalyst increases the content of methyl oleate, which has been known as an ideal component in the biodiesel product, in one reactor unit. Although studies have been conducted on various catalysts for biodiesel production using supercritical fluids, there exist few studies on which processes are most competitive when designing actual processes using these catalysts, especially the biodiesel production process through simultaneous supercritical transesterification and partial hydrogenation (SSTPH). From the comparative study of the biodiesel production processes, the economic feasibility of the biodiesel production process with Pd/Al_2O_3 catalyst was examined.

Second, modeling and dynamic simulation of an aqueous mineral carbonation (MC) process were conducted to prepare the recipe operation of the semi-continuous process. The aqueous mineral carbonation process has a three-phase mixing (solid, liquid, and gas) and complex reactions between them. In this system, complex reactions, phase equilibrium, and heat and material balances are expressed in differential algebraic equations. Finally, the flue gas containing CO_2 comes continuously and irregularly from the power plant and the reactant solution (aqueous $Ca(OH)_2$ solution) is supplied discretely from the

reactant preparation tank. Thus, this multi-phase and multi-component system has a replenishment cycle of the aqueous mineral solution. However, because the metal oxides and carbonates are mixed in the reactor as a slurry, it is difficult to determine whether the mineral reactants are completely consumed. In addition, a large-scale reactor with irregular inputted flue gas is required to ensure sufficient residence time, owing to the low solubility of CO2 in water. Hence, in practical scenarios, the semi-continuous operation is preferred over automatically controlled continuous ones in which the residence time is large and the operational demand is intermittent. Therefore, the MC process in this study was operated under a specific operation recipe (i.e., a sequence of tasks). To improve the existing operation recipes and operational feasibility of the semi-continuous process, two operation recipes are suggested and optimized via Bayesian optimization.

To construct rigorous reaction models for each system, the results from the simulation were compared with the data from lab-scale experiments or pilot-scale plants. The SSTPH processes were not economically estimated, analyzed, and compared before. And the operation recipe for the semi-continuous process was not proposed, analyzed, and optimized before. In such systems, which include a novel reaction mechanism with a new catalyst or the process with an uncommon operation sequence, the proposed methodologies for improving economically and/or operationally feasibility have the potential to be applied to another intensified system.

1.2 Target process descriptions

1.2.1 Biodiesel production process

Biodiesel is a fatty acid methyl esters (FAMEs) made by reacting eco-friendly oils such as vegetable oil, algae oil, and animal fat with alcohol. Biodiesel contains oxygen, which is why it is completely burned and fewer pollutants are released. The conventional biodiesel production process, which has acid/alkali catalysts, has the catalytic neutralization, cleaning, and drying process. In contrast, since the supercritical methanol acts as both a medium and a reactant and the reaction proceeds without a catalyst, no process is needed for catalyst separation or water washing steps. In addition, the simultaneous supercritical transesterification and partial hydrogenation (SSTPH) process decreases the degrees of unsaturation in the biodiesel product without the addition of hydrogen gas, so that the biodiesel product has good cold flow property and oxidation stability. Figure 1 shows the SSTPH reactions and block diagram of the SSTPH process. As shown in Figure 1.(b), the SSTPH process is simplified into five processing units: reactor, methanol recovery, light gases vent system, glycerol separation, and biodiesel purification. Compared to the conventional biodiesel production process, partial hydrogenation, water washing, catalyst separation steps were reduced and also glycerol can be separated easily in the SSTPH process.

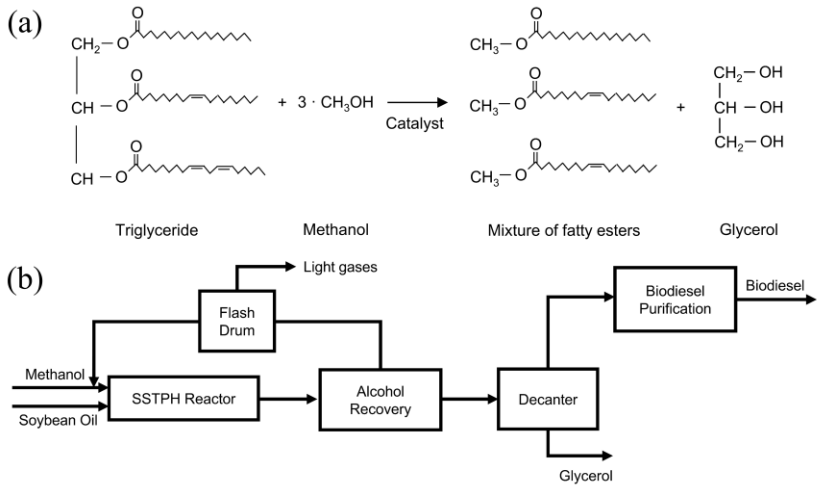

Figure 1 (a) Schematic reaction diagram and (b) block flow diagram of the SSTPH process.

1.2.2 Aqueous mineral carbonation process

Aqueous mineral carbonation (MC) is an effective CCU technology in which CO_2 is reacted with an aqueous metal oxide (e.g., magnesium, calcium, or iron) solution to produce a solid inorganic carbonate that is thermodynamically stabler than CO_2. Three reactions are involved in the aqueous MC process: (1) the dissolution of calcium hydroxide solid particles into a reactant, (2) the mass transfer of carbon dioxide gas into the alkali solution, and (3) ionic reactions between the ions in the aqueous solution (generated through the dissolution of the solid reactant) and CO_2 mass transfer. This process causes the calcium carbonate to precipitate. In general, the rate-determining step of this process is the CO_2 mass transfer and dissolution of $Ca(OH)_2$ (because of its low solubility in water). The representative reactions are expressed as

$$CO_{2(g)} + Ca(OH)_{2(s)} \rightleftarrows CaCO_{3(s)} + H_2O_{(l)}. \quad (1\text{-}1)$$

In the aqueous MC process, the reaction rate and pH level in the reactor rapidly decrease when the mineral reactants in the solution are entirely depleted and the process is operated semi-continuously. As shown in Figure 2, flue gas comes continuously and irregularly from the power plant and the reactant solution is replenished discretely. However, the final purpose of this process is that the overall CO_2 removal efficiency should always be higher than 90% during the operation. Hence, two operation recipes are suggested and optimized via Bayesian optimization to ensure operational feasibility.

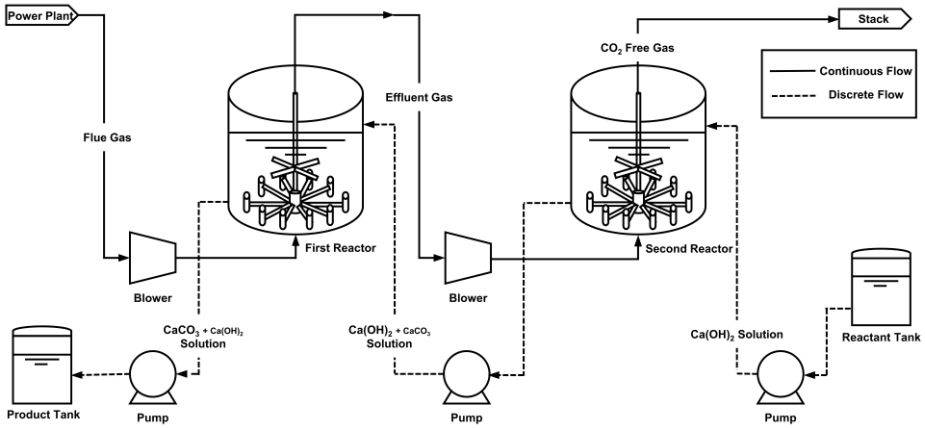

Figure 2 Process flow diagram of the aqueous MC process.

1.3 Outline of the thesis

This thesis consists of five chapters. Chapter 1 explains the research motivation of studying these projects and topics. Furthermore, the thesis outline is listed with associated publications to clarify the relative papers and co-authors. In Chapter 2, a process design and analysis of the biodiesel production process following the general product design strategies with the process intensification approach are included to figure out the economic feasibility of the SSTPH process with Pd/Al_2O_3 catalyst. In Chapter 3, the modeling and validation of an aqueous MC process are conducted to prepare the optimization of semi-continuous operations. In Chapter 4, two operation recipes for an aqueous MC process are suggested and optimized via Bayesian optimization for operational feasibility. Finally, Chapter 5 presents the concluding remarks.

1.4 Associated publications

The work of Chapter 2 is written based on [1]. The works in Chapter 3 and Chapter 4 are presented in [2].

Chapter 2

Economic feasibility study on biodiesel production process

2.1 Introduction

This chapter introduces the comparative study of three biodiesel production processes, which are the conventional non-catalyst supercritical transesterification process, called SC PFR, the simultaneous supercritical transesterification and partial hydrogenation (SSTPH) process with Cu catalyst, called Cu-based PBR, and SSTPH process with Pd/Al_2O_3 catalyst. In the biodiesel production process using supercritical fluids, reactions can proceed with supercritical methanol without a catalyst. Nevertheless, studies have been conducted on the use of several catalysts due to increased reaction rates and improved biodiesel quality. Shin et al. [3] studied the reactions of transesterification and partial hydrogenation simultaneously using Cu catalysts, and Lee et al. [4] have found that Pd/Al_2O_3 and Ni can also play the same role as Cu. In the case of Pd/Al_2O_3 catalyst, hydrogenation occurs well and the FAMEs conversion is maintained high over a wide range of the pressure. The Cu catalyst has a high value of the fatty acid methyl esters (FAMEs) conversion at low pressure and shows a high selectivity of methyl oleate (C18:1). Ni catalyst has a low value of FAMEs conversion but has a high selectivity of C18:1 at low pressures. Using these catalysts increases the selectivity of C18:1 in biodiesel through hydrogenation reactions. Although studies have been conducted on various catalysts for biodiesel production using supercritical

fluids, there exist few studies on which processes are most competitive when designing actual processes using these catalysts, especially the biodiesel production process through SSTPH.

The cold flow property and oxidation stability are some of the important characteristics of biodiesel, which are related to the length of the carbon chain and the number of double bonds. Unsaturation results in good cold flow property and low oxidation stability. Saturation results in good oxidation stability, while less desirable cold flow property. In most cases, it would be impossible to achieve the specified minimum of EN 14214 standard for oxidation stability of 6 hours without using anti-oxidant additives or partial hydrogenation. In contrast, the cold filter plugging point, which is one of the cold flow properties, increases as the decrease of unsaturation. Hence, C18:1 is known as a good material for biodiesel because these two properties are balanced. For the high content C18:1 in the biodiesel product, the expensive raw materials that have a high content of C18:1 such as sunflower oil (34.3%), rapeseed oil (64.4%), and olive oil (75%), are used or the partial hydrogenation process is needed. Here, the increase in the raw material price can lead to an increase in the biodiesel product price, thus, biodiesel cannot be substituted for fossil diesel in price competition. Consequently, the SSTPH process is economically favored in that high content of C18:1 in the biodiesel can be obtained without additional partial hydrogenation process, the addition of hydrogen gases, and the use of expensive raw materials.

The general product design strategies, as shown in Figure 3, with process intensification approach, combining two reactions in one reactor, are conducted

to estimate the economic feasibility of the SSTPH process with Pd/Al_2O_3 catalyst.

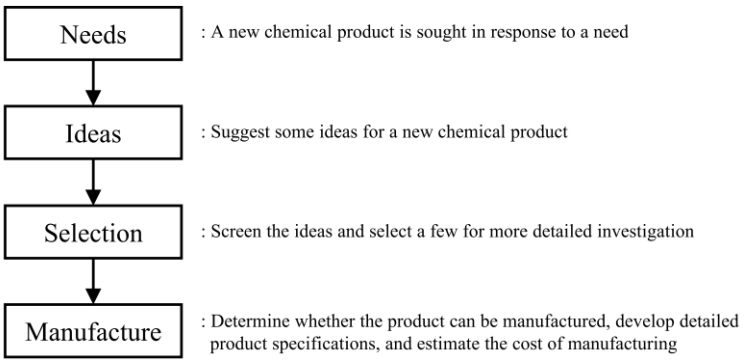

Figure 3 General product design strategies [5].

2.2 Reaction kinetics

The transesterification reaction occurs in three steps, but the overall reaction, a simplified one-step reaction, was considered; that is, the intermediate reactions of diglyceride and monoglyceride were ignored. And methanol is assumed to be a hydrogen source for the hydrogen addition reactions. The SSTPH reactions, which consists of five reactions, are expressed as

$$TG + 3 \cdot M \underset{k_2}{\overset{k_1}{\rightleftharpoons}} GL + 3 \cdot ME, \quad (2\text{-}1)$$

$$MLn + H_2 \underset{k_4}{\overset{k_3}{\rightleftharpoons}} ML, \quad (2\text{-}2)$$

$$ML + H_2 \underset{k_6}{\overset{k_5}{\rightleftharpoons}} MO, \quad (2\text{-}3)$$

$$MO + H_2 \underset{k_8}{\overset{k_7}{\rightleftharpoons}} MS, \quad (2\text{-}4)$$

$$M \underset{k_{10}}{\overset{k_9}{\rightleftharpoons}} 2 \cdot H_2 + CO. \quad (2\text{-}5)$$

where TG is triglyceride, MLn is methyl linolenate, ML is methyl linoleate, MO is methyl oleate, MS is methyl stearate, M is methanol, H2 is hydrogen, CO is carbon monoxide, GL is glycerol, and ME is methyl ester. The reaction rate constants (k_1–k_{10}), which follow the elementary reaction rate equations, corresponding to the forward and reverse of these five reactions, were numbered in order.

The reaction rate constants, which are expressed in the Arrhenius expression, obtained from the experimental data are summarized in Table 1.

Table 1 Kinetic parameters (E, A)

	k_1	k_2	k_3	k_4	k_5
E (J/mol)	110708.5	74032.76	49824.27	58802.44	49809.27
A	419748.6	76.28	13372.88	7.24	15203.99

	k_6	k_7	k_8	k_9	k_{10}
E (J/mol)	68586.24	59135.48	24542.29	54558.03	3517.26
A	78.717	123.04	0.0286	1.51	0.0047

As shown in Table 1, all forward partial hydrogenation reactions, reactions (2-2–2-4), were favored in that they have higher pre-exponential factors (A) and lower activation energies (E) than those of their reverse counterparts. In addition, the more double bonds exist in methyl esters, the faster the partial hydrogenation occurs. In reactions (2-1–2-5) at 300 °C, equilibrium constants, which were estimated by dividing the forward reaction constant by that of the reverse, were approximately 2.78, 12275, 10909, 3.01, and 0.00712, respectively. It showed that high methyl oleate content in FAMEs could be obtained in that the reactions (2-2 and 2-3) have a high equilibrium constant and the equilibrium constant of reaction (2-4) is quite low. Besides, the equilibrium constant of reaction (2-4) is low, but if it is large, methanol would be decomposed much and the molar ratio of methanol to oil would be reduced. Although the reduction of methanol occurs during the reaction, it seems to be negligible for the decrease of FAMEs yield because the ratio was reduced less than 2 and the results were similar to those available in the literature [3, 4].

2.3 Process simulation

In this section, the simulation of the three biodiesel production processes is described. First, a continuous transesterification process, using a plug flow reactor (PFR) with supercritical methanol, called SC PFR, was simulated. Second and third, two SSTPH processes using packed bed reactors (PBRs) were simulated, one using a Cu-based catalyst, called Cu-based PBR, and the other using Pd/Al_2O_3 catalyst, called Pd-based PBR. The plant capacity of the biodiesel production process was assumed to be at 5,000 kg/hr based on 8,000

operating hours per year. The process simulation was conducted using Aspen HYSYS® V11.

The biodiesel production process can be decomposed into five processing units: heating and pressurization of raw materials such as methanol and soybean oil, biodiesel production reactions, methanol recovery, glycerol separation, and biodiesel purification. The process design was adopted based on the work of Zhang et al. [6]. The reaction rates and operating conditions for the SC PFR and Cu-based PBR were based on the studies by He et al. [7] and Shin et al. [3], respectively. The reaction kinetics and operating conditions for the Pd-based PBR were simulated based on the experimental data listed in Table 1. A comparison of the reaction rates between the values from the literature or experiment and simulation was shown in Figure 4. To verify the simulation result, reaction rates were compared between the inlet and outlet of the reactor in mass basis. In the SC PFR case, only the yield of 90% was applied by that of literature [7] owing to the absence of the mass basis information. Figure 4 shows that a comparison of the experimental data [3] and the obtained simulation data in Cu-based PBR and Pd-based PBR, where ME is the methyl ester, FAMEs is the fatty acid methyl esters, MSE indicates the mean squared error, Sim. denotes the results from the simulation, and Exp. denotes the results from the experiment.

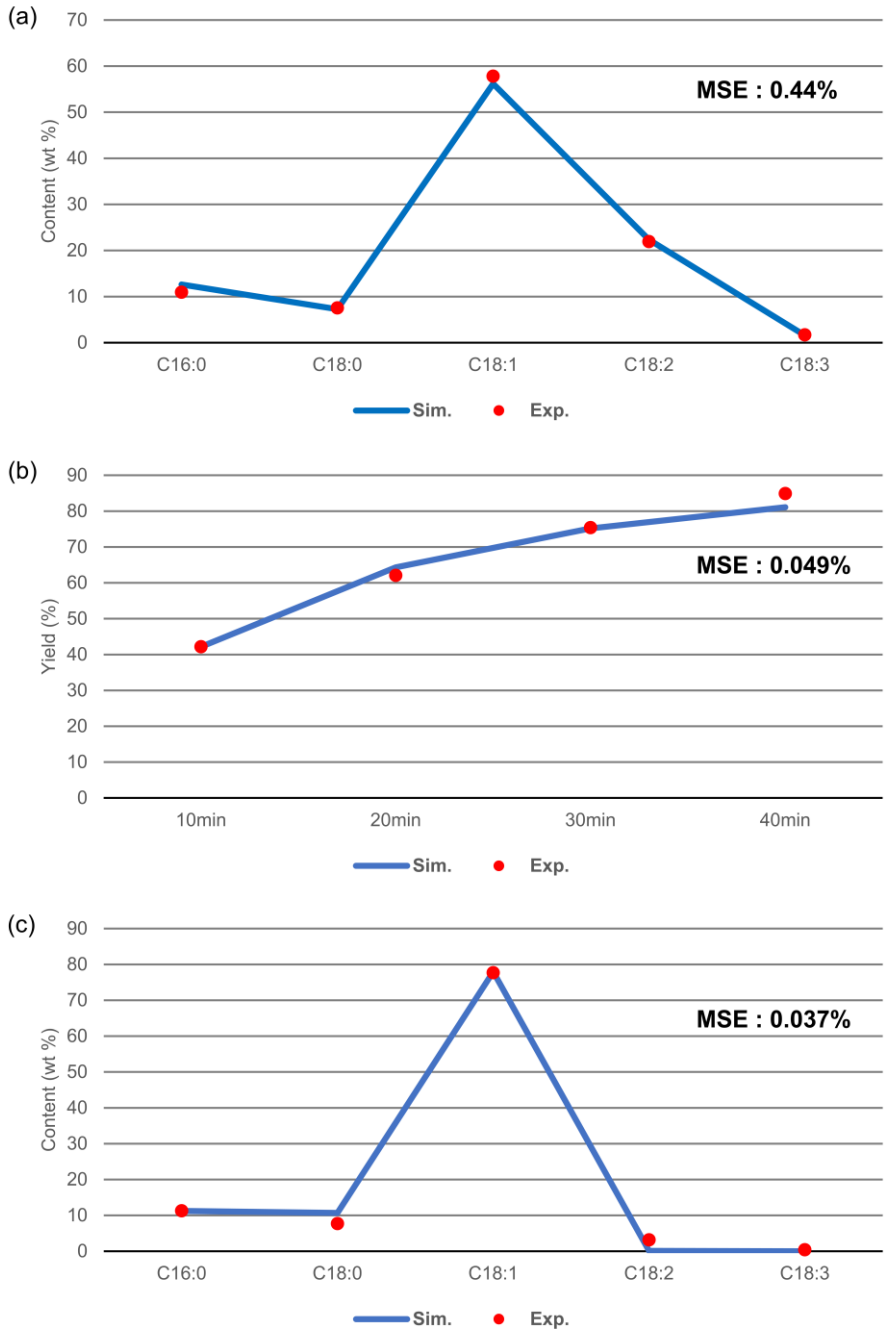

Figure 4 Comparison between experiment and simulation (a) ME contents in the FAMEs (Cu-based PBR), (b) FAMEs Yield (Pd-based PBR), and (c) ME contents in the FAMEs (Pd-based PBR).

The scope of this study was to consider a general configuration of the supercritical biodiesel production process [6, 8–11]; that is, further process integration to reduce the consumption of energy and materials, such as process integration via organic Rankine cycle [11], using a spiral reactor [12], and the addition of co-solvent [13–16], was not considered. In addition, the light gases, which exists as a mixture of CO and H_2, produced by the methanol decomposition in SSTPH could be converted to valuable products such as methanol (by integrating reverse water gas shift reaction), and H_2 (by integrating the steam reforming or water gas shift reaction). Nevertheless, because the main focus in this study was to compare the economic profitability for different degrees of unsaturation of biodiesel product given the same feed oil (soybean oil) and reaction material (supercritical methanol), we decided to choose the general configuration and to ignore the light gas handling for consistency in a comparative study.

2.3.1 Material and thermodynamic model

Soybean oil was used as the raw material shown in Table 2.

Table 2 Contents of soybean oil

Carbon chain number	Chemical name in soybean oil		Chemical name of FAMEs product	Composition (wt%)
16:0	Tripalmitin	Palmitic triglyceride	Methyl palmitate	11.2
18:0	Tristearin	Stearic triglyceride	Methyl stearate	4.2
18:1	Triolein	Oleic triglyceride	Methyl oleate	23.0
18:2	Trilinolein	Linoleic triglyceride	Methyl linoleate	54.3
18:3	Trilinolenin	Linolenic triglyceride	Methyl linolenate	6.4
		Other		0.9
		Total		100.0

Non-random two liquid (NTRL) activity coefficient model was selected as the thermodynamic property package owing to the presence of polar components. To estimate the binary interaction parameters which were not available in the Aspen properties, UNIFAC LLE with phase handling to VLL was used for the separation of two liquid phases between glycerol and FAMEs in the decanter and biodiesel purification [8, 17]. Because activity coefficient model such as NRTL and UNIFAC is not recommended to be used for pressures greater than 10 bar, the Predictive Soave Redlich Kwong (PSRK) equation of state (EOS), which is known as one of the most recommended EOS for handling the sub- and supercritical components of the mixture simultaneously [18], was used in the process unit operations and streams for pressures greater than 10 bar. In particular, the PSRK with phase handling to liquid only was used to prevent and ignore the phase change in the reactor. Figure 5 shows the schematic diagram of thermodynamic property packages. In the change of thermodynamic property package, pressure and enthalpy between upstream and downstream were set to equal for the energy balance.

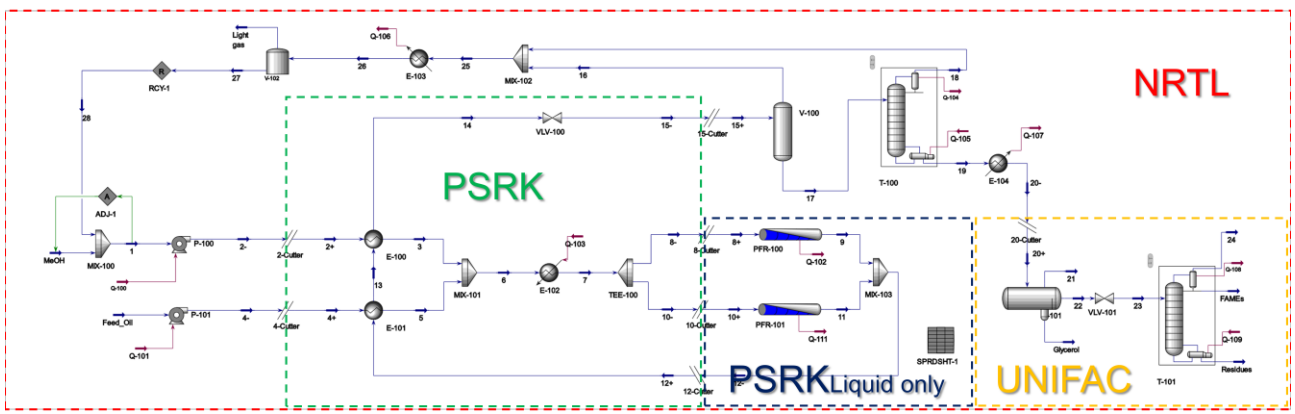

Figure 5 Thermodynamic property packages for biodiesel production process.

2.3.2 Assumptions

- The plant capacity of 5,000 kg/hr with 8,000 operating hours per year.
- The unknown component, which is called Other in Table 2, was ignored.
- The overall conversion rate of triolein was the same as the yield in the literature [3, 7].
- Pressure drop per tray in the column was set to 0.7 kPa and the rest was set to 0 kPa.
- The minimum temperature approach for heat exchanger was set to 10 °C.
- In the change of thermodynamic property package, pressure and enthalpy between upstream and downstream were set to equal.

2.3.3 SC PFR

Figure 6 shows the process flow diagram and stream table of the SC PFR. Methanol (MeOH) and soybean oil (Feed_Oil) were pressurized to reach the reaction pressure (250 bar) using P-100 and P-101, respectively, and preheated through heat exchangers (E-100, E-101, and E-102, respectively) so that the temperature of the reactor inlet reached the reaction temperature (280 °C). Subsequently, methanol and soybean oil streams were mixed in a mixer (MIX-101) and flowed into the supercritical transesterification reactor (PFR-100 and PFR-101). For preventing the diameter of the reactor from exceeding 3 m, the reactant flow was split into two streams and two PFR reactors were used.

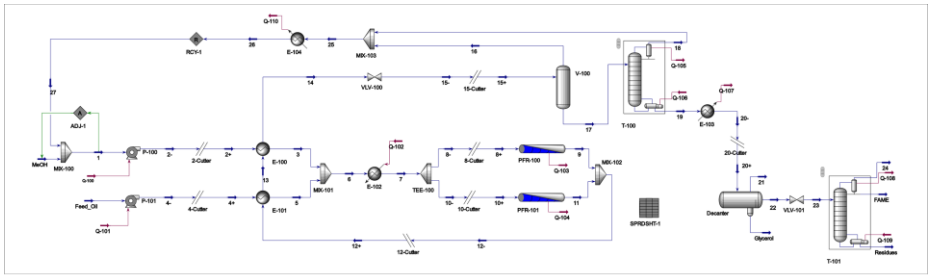

Stream name	Feed Oil	MeOH	7	12+	15+	17	19	Glycerol	22	FAMEs	Residues
Pressure (kPa)	101.3	101.3	25000	25000	103.4	103.4	103.4	103.4	103.4	1.5	3.6
Temperature (℃)	25	25	280	280	69.78	69.78	150	35	35	108.2	250
Molar flow (kgmol/hr)	6.404	19.04	275.4	275.4	275.4	135.4	25.46	7.149	18.31	17.14	0.7662
Mass flow (kg/hr)	5585	610.2	14203	14203	14203	9719	6195	615.2	5580	5000	566.1
Component mass fraction											
TG 16:0	0.1130	0.1130	0.0444	0.0070	0.0070	0.0102	0.0160	0.0180	0.0158	0.0000	0.1554
TG 18:0	0.0424	0.0424	0.0167	0.0033	0.0033	0.0048	0.0075	0.0084	0.0074	0.0000	0.0729
TG 18:1	0.2321	0.2321	0.0913	0.0101	0.0101	0.0148	0.0232	0.0000	0.0257	0.0000	0.2538
TG 18:2	0.5479	0.5479	0.2155	0.0166	0.0166	0.0243	0.0381	0.0428	0.0375	0.0000	0.3701
TG 18:3	0.0646	0.0646	0.0254	0.0023	0.0023	0.0034	0.0053	0.0000	0.0059	0.0000	0.0583
ME 16:0	0.0000	0.0000	0.0000	0.0377	0.0377	0.0550	0.0863	0.0000	0.0958	0.1064	0.0048
ME 18:0	0.0000	0.0000	0.0000	0.0135	0.0135	0.0197	0.0308	0.0000	0.0342	0.0374	0.0070
ME 18:1	0.0000	0.0000	0.0000	0.0815	0.0815	0.1191	0.1869	0.0000	0.2075	0.2292	0.0208
ME 18:2	0.0000	0.0000	0.0000	0.1998	0.1998	0.2919	0.4580	0.0000	0.5084	0.5617	0.0497
ME 18:3	0.0000	0.0000	0.0000	0.0232	0.0232	0.0339	0.0531	0.0000	0.0590	0.0650	0.0074
Glycerol	0.0000	0.0000	0.0000	0.0374	0.0374	0.0546	0.0856	0.8603	0.0002	0.0002	0.0000
Methanol	0.0000	0.0000	0.6068	0.5678	0.5678	0.3684	0.0092	0.0704	0.0024	0.0001	0.0000
H_2	0.0000	0.0000	0.0000	0.0000	0.0000	0.0000	0.0000	0.0000	0.0000	0.0000	0.0000
CO	0.0000	0.0000	0.0000	0.0000	0.0000	0.0000	0.0000	0.0000	0.0000	0.0000	0.0000

Figure 6 Process flow diagram and stream table of SC PFR.

Table 3 Reaction summary in SC PFR

SC PFR					
Pressure (bar)			250		
Temperature (°C)			280		
Methanol : Soybean oil (molar)			42:1		
Residence Time (min)			30		
Reactor Type			PFR		
Catalyst			None		
	C16:0	C18:0	C18:1	C18:2	C18:3
k (s^{-1})	8.33E-04	6.59E-04	9.11E-04	1.08E-03	1.01E-03
Yield (%)			90		

In the SC PFR, the reaction condition and yield were obtained from the study by He et al. [7], where the reaction temperature of 280 °C and pressure of 250 bar. Table 3 represents the summary of the reactions in the SC PFR.

After the reactions, the reactor effluent stream contained excess methanol, glycerol, unreacted soybean oil, and the biodiesel product. The purified biodiesel was obtained through three separation steps: methanol recovery, glycerol separation, and biodiesel purification.

First, a flash evaporator (V-100) and a five theoretical stages distillation column (T-100) were used to recover the excess methanol. The valve (VLV-100) was used to depressurize the reactor effluent stream from 25,000 kPa to 103.4 kPa in order to separate a significant portion of the methanol through the flash evaporator. The remaining methanol was further separated using the five-stage distillation column. The methanol recovery column is operable at the atmospheric pressure, but needs to be operated below 150 °C in order to avoid the glycerol thermal decomposition [19]. After determining the minimum number of stages using a shortcut design method and the final number of stages based on Gilliland correlation [20], case studies were conducted by manipulating the reflux ratio, and the number of total stages and the feed stage location to minimize the energy consumption. Consequently, 99.24% of the methanol in the reactor effluent stream was recovered through this procedure and mixed with fresh make-up methanol (MeOH stream). A cooler (E-104) was used to liquify the methanol to nullify the presence of vapor in the pump. After the methanol recovery step, the bottom of the distillation column T-100, including glycerol, unreacted soybean oil, and the biodiesel product, was

cooled to 35°C. As a result, two liquid phases were formed: the glycerol-rich phase and the biodiesel phase. The glycerol was separated as a byproduct using a decanter (Decanter). Finally, the biodiesel was refined using another five-stage distillation column (T-101) to satisfy the requirement of the maximum free glycerol content (≤0.02wt%) according to ASTM D6751. Because FAMEs are susceptible to thermal decomposition above 250 °C [21], the top pressure of T-101 was set to 1.5 kPa to keep the temperature at a suitably low value. After determining the number of minimum stages similar to the methanol recovery column, case studies for the biodiesel purification column were also conducted. From the case studies, useful correlations were identified: first, the amount of biodiesel product was increased as the number of stages was reduced; second, the content of biodiesel in the bottoms was increased with the increase of the bottom temperature. However, for preventing thermal decomposition of FAMEs, the temperature of the bottoms was set to 250 °C; finally, the lower location of the feed stage, except for the reboiler, gave the less content of FAMEs in the bottom stream. As a result, 99.97% purified biodiesel could be obtained through the five-stage distillation column, and the degree of unsaturation was similar to that of soybean oil.

2.3.4 Cu-based PBR

Figure 7 shows the process flow diagram and stream table of the Cu-based PBR. Methanol and soybean oil were also pressurized, preheated, and mixed in the same manner as in the SC-PFR. Then, a heater (E-102) was used to increase the temperature to 320 °C, and the reactant stream flowed into the SSTPH reactor (CRV-100 and CRV-101).

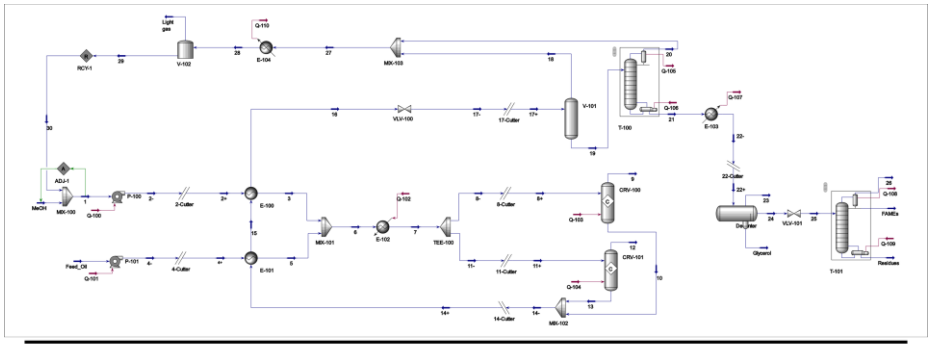

Stream name	Feed Oil	MeOH	7	14+	17+	19	21	Light gas	Glycerol	24	FAME	Residues
Pressure (kPa)	101.3	101.3	20000	20000	103.4	103.4	103.4	101.3	103.4	103.4	1.5	3.6
Temperature (℃)	25	25	320	320	67.71	67.71	150	35	35	35	118	250
Molar flow (kgmol/hr)	6.46	33.85	297.3	305.8	305.8	125	25.74	23.20	7.187	18.55	17.1	1.014
Mass flow (kg/hr)	5634	1085	14951	14951	14951	9448	6267	452.3	604.7	5663	5001	646.7
Component mass fraction												
TG 16:0	0.1130	0.0000	0.0426	0.0028	0.0028	0.0045	0.0068	0.0000	0.0076	0.0067	0.0000	0.0587
TG 18:0	0.0424	0.0000	0.0160	0.0132	0.0132	0.0209	0.0316	0.0000	0.0355	0.0311	0.0000	0.2727
TG 18:1	0.2321	0.0000	0.0875	0.0030	0.0030	0.0047	0.0072	0.0000	0.0000	0.0079	0.0000	0.0693
TG 18:2	0.5479	0.0000	0.2065	0.0000	0.0000	0.0000	0.0000	0.0000	0.0000	0.0000	0.0000	0.0000
TG 18:3	0.0646	0.0000	0.0243	0.0177	0.0177	0.0281	0.0423	0.0000	0.0000	0.0469	0.0000	0.4102
ME 16:0	0.0000	0.0000	0.0000	0.0399	0.0399	0.0632	0.0953	0.0000	0.0000	0.1054	0.1275	0.0108
ME 18:0	0.0000	0.0000	0.0000	0.0254	0.0254	0.0402	0.0605	0.0000	0.0000	0.0670	0.0708	0.0276
ME 18:1	0.0000	0.0000	0.0000	0.1949	0.1949	0.3084	0.4649	0.0000	0.0000	0.5146	0.5611	0.1061
ME 18:2	0.0000	0.0000	0.0000	0.0770	0.0770	0.1218	0.1836	0.0000	0.0000	0.2032	0.2232	0.0409
ME 18:3	0.0000	0.0000	0.0000	0.0054	0.0054	0.0086	0.0130	0.0000	0.0000	0.0144	0.0158	0.0037
Glycerol	0.0000	0.0000	0.0000	0.0359	0.0359	0.0568	0.0857	0.0000	0.8857	0.0003	0.0006	0.0000
Methanol	0.0000	1.0000	0.6230	0.5679	0.5679	0.3427	0.0091	0.4518	0.0711	0.0025	0.0009	0.0000
H_2	0.0000	0.0000	0.0000	0.0012	0.0012	0.0000	0.0000	0.0383	0.0000	0.0000	0.0000	0.0000
CO	0.0000	0.0000	0.0002	0.0156	0.0156	0.0000	0.0000	0.5099	0.0000	0.0000	0.0000	0.0000

Figure 7 Process flow diagram and stream table of Cu-based PBR.

In the Cu-based PBR, the reaction condition and conversion rates were obtained from the study by Shin et al. [3] with a reaction yield of 90%. Table 4 represents the summary of the reactions in the Cu-based PBR, where TG is the triglyceride, ME is the methyl ester, GL is the glycerol and M is the methanol. To match the mass fraction and yield in the literature [3], the conversion rate of the fourth reaction (18:2TG + M → GL + 3·18:2ME) was set to 100%; otherwise, some reaction conversion rate would not be between 0 and 1.

As the hydrogenation reaction produced light gases such as H_2 and CO, a flash drum (V-102) was added after the methanol recovery. In addition, because the loss of methanol in the light gases was reduced as the decrease of temperature, a cooler (E-104) was used to reduce the temperature to 35 °C. The light gases were separated from the excess methanol recycle stream to prevent the presence of the gas phase in the pump. As a result, the methanol recovery efficiency decreased to 96.93%. The other separation steps were identical to those of the SC PFR, and 99.97% purified biodiesel was obtained. Unlike the SC PFR, the degree of unsaturation decreased owing to the partial hydrogenation. As shown in the stream table of Figure 7, the content of methyl oleate (18:1ME) in the product (FAME stream) was increased compared to that in the SC PFR.

Table 4 Reaction summary in Cu-based PBR

Cu-based PBR						
Pressure (bar)	200					
Temperature (°C)	320					
Methanol : Soybean oil (molar)	45:1					
Residence Time (min)	30					
Reactor Type	PBR					
Catalyst	Cu					
	C16:0	C18:0	C18:1	C18:2	C18:3	Others
Content of Fatty Acid in Soybean oil (wt%)	10.4	4.4	24.6	52.5	6.8	1.3
Content of Methyl Ester in FAMEs (wt%)	10.3	7.1	54.3	20.6	1.6	6.1
Yield (%)	90					
Class	Reaction					Conversion (molar %)
Transesterification	16:0TG + M → GL + 3 · 16:0ME					93.31
	18:0TG + M → GL + 3 · 18:0ME					17.15
	18:1TG + M → GL + 3 · 18:1ME					96.57
	18:2TG + M → GL + 3 · 18:2ME					100
	18:3TG + M → GL + 3 · 18:3ME					27.08
Hydrogenation	18:3ME + H_2 → 18:2ME					17.81
	18:2ME + H_2 → 18:1ME					63.10
	18:1ME + H_2 → 18:0ME					10.34
Methanol decomposition	M → 2 · H_2 + CO					2.832

2.3.5 Pd-based PBR

Figure 8 shows the process flow diagram and stream table of the Pd-based PBR. Methanol and soybean oil were pretreated in the same manner as in the Cu-based PBR.

In the Pd-based PBR, the reaction condition and kinetics were simulated based on the experimental data described in the previous section. Table 5 summarizes the reactions in the Pd-based PBR, and the separation steps were the same as those of the Cu-based PBR. The methanol recovery efficiency was 94.88%, which was higher than that of the Cu-based PBR owing to the high partial hydrogenation. After the separation steps, 99.97% purified biodiesel was obtained. Similar to the Cu-based PBR, the content of methyl oleate (18:1ME) in the product (FAME stream) was higher than that of the SC PFR, but much higher than that of the Cu-based PBR.

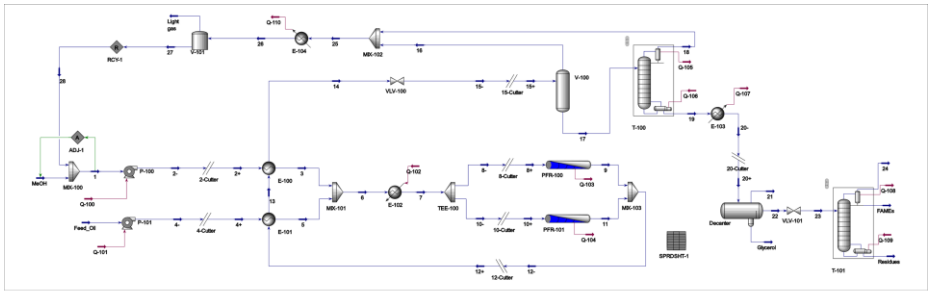

Stream name	Feed Oil	MeOH	7	12+	15+	17	19	Light gas	Glycerol	22	FAME	Residues
Pressure (kPa)	101.3	101.3	10000	10000	103.4	103.4	103.4	101.3	103.4	103.4	1.5	3.6
Temperature (℃)	25	25	300	300	67.49	67.49	150	35	35	35	125.1	250
Molar flow (kgmol/hr)	6.49	44.98	298.6	314.8	314.8	101.7	25.48	42.16	7.104	18.38	17.06	0.8743
Mass flow (kg/hr)	5660	1441	15020	15020	15020	8735	6294	807.5	620.1	5674	5001	656.9
Component mass fraction												
TG 16:0	0.1130	0.0000	0.0426	0.0426	0.0426	0.0084	0.0117	0.0000	0.0131	0.0116	0.0000	0.1000
TG 18:0	0.0424	0.0000	0.0160	0.0160	0.0160	0.0032	0.0044	0.0000	0.0049	0.0043	0.0000	0.0375
TG 18:1	0.2321	0.0000	0.0875	0.0875	0.0875	0.0174	0.0241	0.0000	0.0000	0.0267	0.0000	0.2309
TG 18:2	0.5479	0.0000	0.2065	0.2065	0.2065	0.0410	0.0568	0.0000	0.0635	0.0561	0.0000	0.4848
TG 18:3	0.0646	0.0000	0.0243	0.0243	0.0243	0.0048	0.0067	0.0000	0.0000	0.0074	0.0000	0.0642
ME 16:0	0.0000	0.0000	0.0000	0.0000	0.0000	0.0651	0.0904	0.0000	0.0000	0.1002	0.1132	0.0032
ME 18:0	0.0000	0.0000	0.0000	0.0000	0.0000	0.0619	0.0859	0.0000	0.0000	0.0953	0.1063	0.0133
ME 18:1	0.0000	0.0000	0.0000	0.0000	0.0000	0.4511	0.6260	0.0000	0.0000	0.6944	0.7789	0.0660
ME 18:2	0.0000	0.0000	0.0000	0.0000	0.0000	0.0007	0.0009	0.0000	0.0000	0.0010	0.0012	0.0001
ME 18:3	0.0000	0.0000	0.0000	0.0000	0.0000	0.0000	0.0001	0.0000	0.0000	0.0001	0.0001	0.0000
Glycerol	0.0000	0.0000	0.0000	0.0000	0.0000	0.0605	0.0840	0.0000	0.8502	0.0003	0.0002	0.0000
Methanol	0.0000	1.0000	0.6230	0.6230	0.6230	0.2859	0.0090	0.4599	0.0682	0.0025	0.0001	0.0000
H_2	0.0000	0.0000	0.0000	0.0000	0.0000	0.0000	0.0000	0.0403	0.0000	0.0000	0.0000	0.0000
CO	0.0000	0.0000	0.0002	0.0002	0.0002	0.0000	0.0000	0.4998	0.0000	0.0000	0.0000	0.0000

Figure 8 Process flow diagram and stream table of Pd-based PBR.

Table 5 Reaction summary in Pd-based PBR

Pd-based PBR	
Pressure (bar)	100
Temperature (°C)	300
Methanol : Soybean oil (molar)	45 : 1
Residence Time (min)	40
Reactor Type	PBR
Catalyst	Pd/Al_2O_3

2.4 Economic analysis

Previous studies on economic analysis, based on the Lang or Guthrie methods (Kasteren and Nisworo et al. [22], You et al. [23], Lim et al. [9], Kelloway et al. [24], Sakdasri et al. [25]), which provide approximate cost factors, have relatively poor accuracies of estimation for new processes, such as the SSTPH processes (Turton et al. [26]). Consequently, the Aspen Process Economic Analyzer V11, which provides investment parameters and economic data for capital and operating cost estimation, was used for a more accurate estimation (Seider et al. [27], Lee et al. [10]). The equipment type and size of each process unit were determined based on the Aspen HYSYS process model. Carbon steel was chosen as the base material of construction (MOC) owing to the absence of a strong acid material, and stainless steel was used for the pumps, heat exchangers, and reactor at high pressure and temperature. The amount of catalyst for the Cu-based PBR and the Pd-based PBR was fixed at 10 wt% of soybean oil considering the residence time of each process.

Table 6 present the equipment summary for each process, where L-L means Liquid-Liquid separator and Hor. means the horizontal orientation. For the distillation columns, "Duty (Con./Reb.)" denotes the duty of the condenser and reboiler. The investment parameters are summarized in Table 7. Table 8 lists the prices of the raw materials, products, and catalysts used in this study. The averages of the prices of soybean oil, methanol, and biodiesel product from November 2019 to October 2020 were used.

Table 6 Equipment summary for three biodiesel production processes

	SC PFR					Cu-based PBR					Pd-based PBR				
Pumps	P-100		P-101			P-100		P-101			P-100		P-101		
Type	Centrifugal														
Efficiency	75														
MOC	SS316														
Flow (kg/hr)	8618		5585			9317		5634			9360		5660		
P in (kPa)	101.3														
P out (kPa)	2.5E4					2E4					1E4				
Driver power (kW)	106.4		56.20			87.79		45.31			43.85		22.64		
Heat exchangers	E-100	E-101	E-102	E-103	E-104	E-100	E-101	E-102	E-103	E-104	E-100	E-101	E-102	E-103	E-104
Type	TEMA shell&tube														
Area (m^2)	23.04	12.23	67.21	15.19	53.83	25.74	32.16	52.57	14.89	138.3	45.18	17.59	193.7	20.17	133.0
MOC	321S			CS		321S			CS		321S			CS	
Duty (kW)	714.2	648.1	1352	421.8	2458	1288	912	1688	436.4	2748	1431	825.7	1814	451.1	2650
Shell in (°C)	238	280	-	-	-	269.2	320	-	-	-	257	300	-	-	-
Shell in (kPa)	2.5E4		-	-	-	2E4		-	-	-	1E4		-	-	-
Tube in (°C)	84.55	10.23	182.9	150	67.48	51.81	16.6	217.2	150	66.56	49.2	29.09	209	150	66.68
Tube in (kPa)	2.5E4			103.4	101.3	2E4			103.4	101.3	1E4			103.4	101.3
Reactors	PFR-100 & PFR-101					CRV-100 & CRV-101					PFR-100 & PFR-101				
Type	Plug flow					Packed bed					Packed bed				
Orientation	Horizontal														
MOC	SS316														
T (°C)	280					300					300				
P (kPa)	2.5E4					2E4					1E4				
Residence time (min)	30					30					40				
Diameter (m)	1.830					2.002					2.482				
Height/length (m)	5.491					6.007					7.447				
Catalyst (kg)	-					140.8					187.8				
Separators	V-100	Dec.	T-100	T-101		V-101	V-102	Dec.	T-100	T-101	V-101	V-102	Dec.	T-100	T-101
Application	Knock-out	L-L	Distillation			Knock-out		L-L	Distillation		Knock-out		L-L	Distillation	
Orientation	Vertical	Hor.	Vertical			Vertical		Hor.	Vertical		Vertical		Hor.	Vertical	
# of stages	-	-	5	5		-	-	-	5	5	-	-	-	5	5
MOC	CS														
Duty (kW) (Cond./Reb.)	-	-	-10.8 /1369	-757.4 /1035		-	-	-	-68.1 /1350	-733 /1062	-	-	-	-44.8 /1109	-721 /1081

Table 7 Investment parameters for the three biodiesel production processes

Name	Value	Unit
Economic life of project	10	Year
Tax rate	40	%/year
Interest rate/Desired rate of return	20	%/year
Salvage value	0	% of initial capital cost
Depreciation method	Straight line	
Escalation parameters		
Project capital escalation	5	%/year
Products escalation	5	%/year
Raw material escalation	3.5	%/year
Operating & maintenance labor escalation	3	%/year
Utilities escalation	3	%/year
Project capital parameters		
Working capital percentage	15	%/year
Operating costs parameters		
Operating supplies	10	$/year
Laboratory charges	16.3	$/year
Operating charges	25	%/year
Plant overhead	50	%/year
G&A expenses	15	%/year
Facility operation parameters		
Facility type	Chemical processing facility	
Operating mode	Continuous Processing – 24hours	
Plant location	North America	
Length of start-up period	20	Weeks
Operating hours per period	8000	Hours/year
Process fluids	Liquids and gasses	

Table 8 Prices of raw materials, products, and catalysts

Name	Price ($/tonne)
Soybean oil	663.225 [28]
Methanol	246.193 [29]
Biodiesel – FAMEs	881.925 [30]
Glycerol	860 [31]
Pd/Al_2O_3	$0.533 \cdot 10^7$ [32]
Cu	$0.406 \cdot 10^6$ [33]

2.4.1 Total capital investment

Table 9 shows the total capital cost for each biodiesel production process. The cost of methanol recovery and biodiesel purification in the column included the cost of the distillation column, condenser, distillate accumulator, reflux pump, and reboiler. Because the Pd-based PBR had the highest residence time in the reactor and the highest price of catalyst, the costs of the reactor and catalyst were the highest at $1.54 million and $2.00 million, respectively. The SC PFR had the highest cost for the pumps ($8.57 million) and heat exchangers ($9.84 million) owing to the high reaction pressure. Most of the cost categories in the SC PFR were the highest, excluding the costs of the reactor, catalyst, and flash evaporator. This is because the SSTPH processes had the additional vent systems for light gases compared to the SC PFR. In addition, the lower molar ratio of oil to methanol in SC PFR lowered the reactor size and cost. Comparing the SSTPH processes, most of the cost categories in the Cu-based PBR were higher than that of Pd-based PBR. This is because the reaction temperature and pressure in the Cu-based PBR were higher than those in the Pd-based PBR. Consequently, the total capital investment, which is the adjusted total project cost according to the report of the Aspen Process Economic Analyzer, of the Pd-based PBR was the lowest at $15.8 million and approximately half of that of the SC PFR ($29.4 million).

Table 9 Total capital investment for each biodiesel production process at the capacity of 40,000 tonnes/yr (10^6)

Type	Description	SC PFR	Cu-based PBR	Pd-based PBR
Reactor	PFR/PBR	1.10	1.14	1.54
	Catalyst	-	0.114	2.00
Column	Methanol recovery	0.507	0.561	0.538
	Biodiesel purification	0.954	0.963	0.981
Other	Pumps	8.57	4.65	0.998
	Heat exchangers	9.84	7.65	3.612
	L-L separator	0.135	0.134	0.135
	Flash evaporator	0.148	0.496	0.497
Project capital cost	Purchased equipment	5.791	3.74	1.83
	Equipment setting	0.049	0.042	0.031
	Piping	9.81	7.71	3.56
	Civil	0.147	0.260	0.269
	Steel	0.126	0.137	0.143
	Instrumentation	1.12	1.05	1.05
	Electrical	0.808	0.633	0.613
	Insulation	0.227	0.269	0.285
	Paint	0.043	0.052	0.051
	Other	9.30	5.90	6.97
	G&A overheads	0.741	0.516	0.368
	Contract fee	1.17	0.736	0.591
	Contingencies	5.28	3.79	2.84
	Total project cost	34.6	24.8	18.6
	Total capital investment	29.4	21.0	15.8

2.4.2 Total manufacturing cost

Figure 9 shows the total manufacturing cost for each biodiesel production process. Because the methanol was used as the hydrogen donor in the processes of the PBR, the total manufacturing cost in the SC PFR was $37.48 million/y, which was lower than that of the Cu-based PBR ($39.03 million/y) and the Pd-based PBR ($38.97 million/y). The costs of electricity, supervision, and maintenance in the SC PFR were highest at $0.18 million/y, $0.18 million/y, and $0.28 million/y, respectively, owing to the high operating pressure. However, the cost of methanol was the lowest at $1.20 million/y because methanol was used as the hydrogen donor in the processes of the SSTPH. In addition, the ratio between methanol and soybean oil was the lowest at 42:1 in the SC PFR. Because the Pd-based PBR had the lowest yield and methanol recovery efficiency, the cost of raw materials was highest at $32.97 million/y. As shown in Figure 9, the cost of soybean oil accounted for the major proportion of the total manufacturing cost; therefore, the total manufacturing cost of SC PFR ($37.48 million/y) was lower than that of the Cu-based PBR ($39.03 million/y) and Pd-based PBR ($38.97 million/y).

The revenues from the biodiesel and glycerol for each process were $39.51 million/y, $39.44 million/y, and $39.55 million/y, respectively. Although the high content of methyl oleate in the biodiesel product is known to have good cold flow property and oxidation stability, the price of the biodiesel product (FAMEs) is determined only by the degree of blending, if qualified according to EN14214 and ASTM D6751. Therefore, although the cost of methanol increased due to the partial hydrogenation reaction in the cases of the PBR, the revenues from three biodiesel production processes were similar.

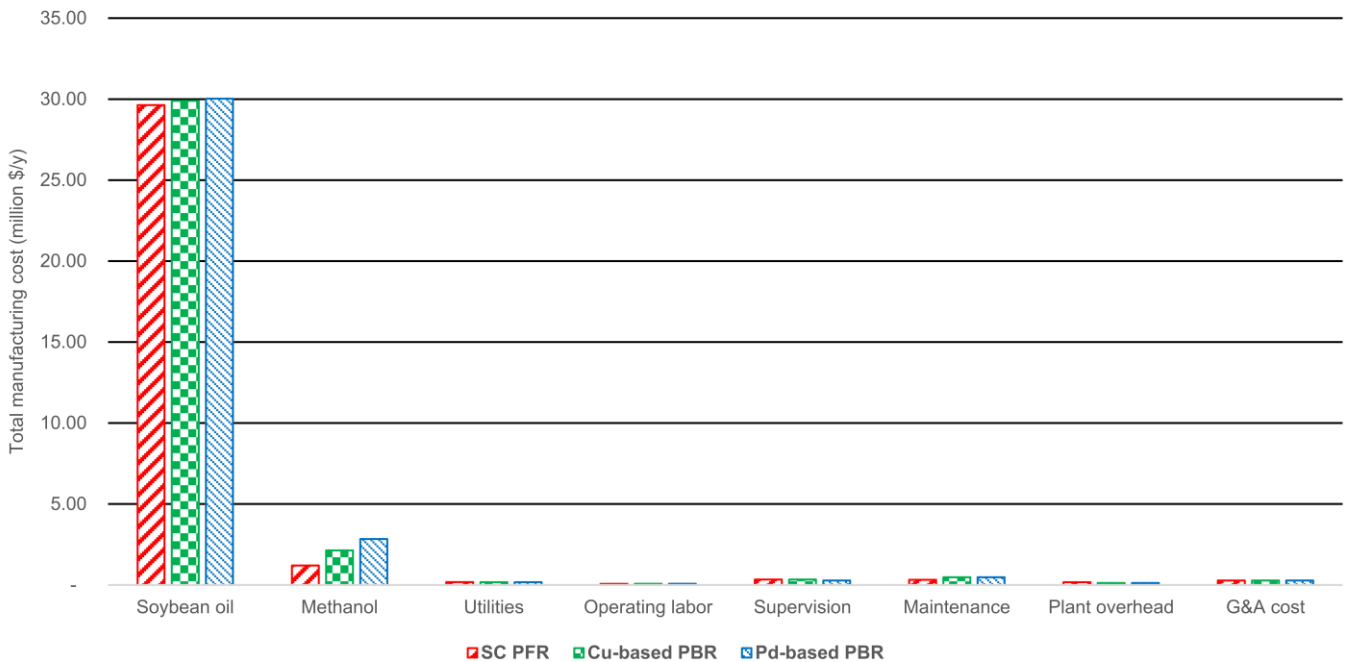

Figure 9 The proportions of subitems in the total manufacturing cost for each biodiesel production process.

2.4.3 Sensitivity analysis

Figure 10 shows the results of the sensitivity analysis. In order to investigate the sensitivity of the net present values (NPVs) for the three biodiesel production processes according to price variation, the prices of soybean oil, methanol, biodiesel product, and glycerol were varied by ±25%, ±50%, and ±75% from the original values shown in Table 8. In addition, the sensitivity analysis was conducted with the production capacity of 1 tonne/hr according to the price variation of biodiesel product. Not all the biodiesel production processes could pay off the investment if the prices did not change. With the price decrease of soybean oil or increase of biodiesel product, three biodiesel production processes made a profit within 10 years.

The slopes of the biodiesel production processes, according to the price change of the biodiesel product, were 1.1496, 1.2006, and 1.2161, respectively. The slopes of the biodiesel production processes, according to the price change of soybean oil, were -1.1255, -1.1998, and -1.2205, respectively. As shown in Figures 10 and the slopes of the biodiesel production processes according to the price change of the biodiesel product and soybean oil, the NPVs are the most sensitive to the price of the biodiesel product. If the price of high methyl oleate biodiesel increases, the NPVs of the SC PFR would be much lower than those of the others. This is because the SC PFR would have the highest total capital investment. In addition, if the slopes of the PBR cases increase, according to the price change of the biodiesel product, increase, the slope of the Pd-based PBR becomes the highest. Nevertheless, the economic profitability of Pd-based PBR was highest in that the break-even biodiesel prices of three biodiesel production processes were 1121 $/tonne, 1116 $/tonne, and 1099 $/tonne,

respectively; that is, although the configuration of three biodiesel production processes was not integrated with advanced technologies to reduce the energy and material consumptions, the payout period would be within 10 years if the biodiesel price were increased by 27.16 %, 26.48 %, and 24.6 %, respectively. The payout period for the 25% decrease of soybean oil price in each case was 9.26, 8.58, and 7.47 years, respectively.

In Figure 9, NPVs were decreased over three biodiesel production processes and only had a positive value with a 75% increase in the price of biodiesel product. The break-even biodiesel prices of three biodiesel production processes were 1510 $/tonne, 1457 $/tonne, and 1366 $/tonne, respectively. The payout periods for each case with a 25 % increase in biodiesel price were 9.3, 8.96, and 7.95 years, respectively. The results showed that the plant capacity of the biodiesel production process has a significant potential for economic profitability. This is because, as shown in Figures 9 and 10, the economic profitability of the supercritical biodiesel production process was highly dependent on the cost for the raw material (especially feed oil) and biodiesel product. In other words, the difference between the cost of feed oil and the revenue of biodiesel would be increased along with the increase in plant capacity. In addition, another major key to increase economic profitability in the biodiesel production process is the reaction condition. As mentioned earlier, the total capital investments for three biodiesel production processes were highly dependent on the reaction temperature and pressure. Consequently, the economic analysis showed that Pd-based PBR had two advantages compared to SC PFR and Cu-based PBR: first, the highest content of methyl oleate in biodiesel product was obtained in SSTPH with Pd/Al_2O_3 catalyst with a high

yield (approximately 88.36%). This could contribute to the increase of biodiesel revenue if the biodiesel price is determined by the degree of unsaturation; second, the mild reaction condition in SSTPH with Pd/Al_2O_3 catalyst reduces the total capital investment, which results in the decrease of payout period and break-even price of biodiesel.

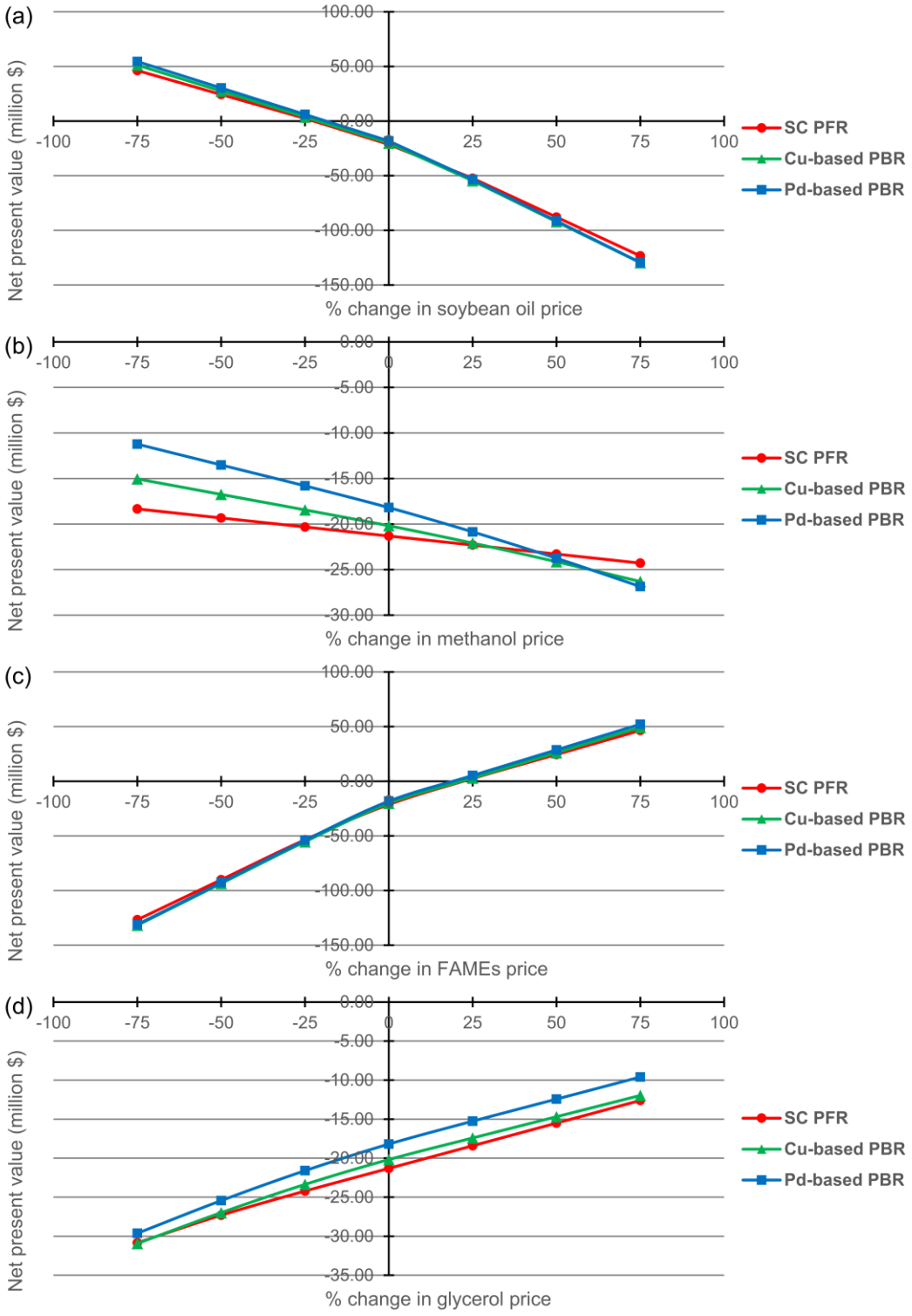

Figure 10 Sensitivities of the NPVs of each biodiesel production process to the price of (a) soybean oil, (b) methanol, (c) FAMEs, and (d) glycerol.

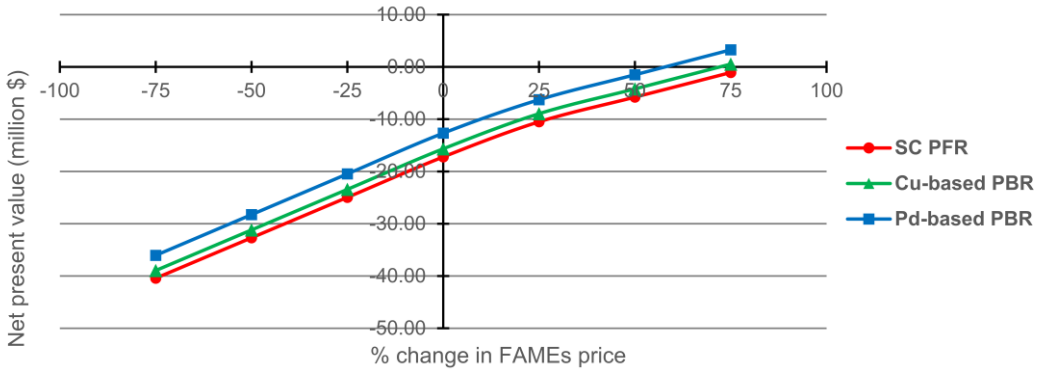

Figure 11 Sensitivity of the NPVs of each biodiesel production process to the production capacity of 1tonne/hr.

2.5 Summary

Process design and economic analysis were conducted to investigate the profitability of the SSTPH process with Pd/Al_2O_3 catalyst in comparison with the supercritical transesterification process, called the SC PFR, and the SSTPH process with a different catalyst, called Cu-based PBR. The process design and simulation models for the three types of biodiesel production processes were developed using Aspen HYSYS V11 and were generally similar, except for the additional vent system for light gases owing to the partial hydrogenation reactions in the Cu-based PBR and Pd-based PBR. The simulation results using Aspen HYSYS V11 for all the cases showed that the 99.97 wt% purity of biodiesel product was obtained.

The economic analyses of the three biodiesel production processes were performed using Aspen Process Economic Analyzer V11 based on the process simulation models developed in Aspen HYSYS V11. It was found that the total capital investment for the Pd-based PBR was the lowest and approximately half of that of the SC PFR, despite the high costs of the reactor and catalyst. The total manufacturing cost for the Pd-based PBR was higher than that for the SC PFR and lower than that for the Cu-based PBR, but the revenues from the biodiesel product and glycerol for each process were similar. Not all the biodiesel production processes could pay off the investment. The results from the sensitivity analysis show that the NPVs for the three biodiesel production processes were most sensitive to the price of the biodiesel product. However, although the degree of unsaturation and methanol consumption were different for each biodiesel production process owing to the partial hydrogenation, the price of the biodiesel product was the same. Nevertheless, the SSTPH with

Pd/Al2O3 catalyst was most profitable for two reasons: One is that the mild reaction condition under Pd/Al_2O_3 catalyst reduced total capital investment; Another is that the high content of methyl oleate in the biodiesel product was obtained with a high reaction yield (approximately 88.36%).

Finally, the SSTPH process could still be further intensified by heat integration, novel reactor or distillation column, and sustainability study. Such intensification of the biodiesel production process and its sustainability assessment could be one of our future studies. Nevertheless, we anticipate that the Pd-based PBR is much more profitable than the others if the price of the biodiesel product is determined by the degree of unsaturation. In addition, without the classification of the biodiesel price, the break-even price of biodiesel in Pd-based PBR was lower (1,099 $/tonne) than those of the SC PFR (1,121 $/tonne) and Cu-based PBR (1,116 $/tonne).

Chapter 3

Modeling and validation of pilot-scale aqueous mineral carbonation process

3.1 Introduction

This chapter introduces the modeling of an aqueous mineral carbonation (MC) process using Aspen Custom Modeler (ACM) V10, which is used to obtain some physical properties of the mixture such as diffusivity of CO_2 and OH^- ion in an aqueous electrolyte solution and the kinematic viscosity of the liquid. The process in this study is a pilot-scale carbonation process that captures 40 tons of CO_2 per day using a 20 wt% aqueous solution of calcium hydroxide. The flue gas (containing 15 vol% CO_2) is obtained from a power plant. For model validation, the results from the dynamic simulation were compared with the actual pilot-plant operation data.

3.2 Reaction kinetics

Three reactions are involved in the aqueous MC process: (1) the dissolution of calcium hydroxide solid particles into a reactant, (2) the mass transfer of carbon dioxide gas into the alkali solution, and (3) ionic reactions between the ions in the aqueous solution (generated through the dissolution of the solid reactant) and CO2 mass transfer. This process causes the calcium carbonate to precipitate. In general, the rate-determining step of this process is the CO2 mass transfer and dissolution of Ca(OH)2 (because of its low solubility in water).

3.2.1 Calcium hydroxide dissolution in water

The reaction mechanism for calcium hydroxide dissolution includes two steps: forward and backward reactions. These are expressed as

$$Ca(OH)_2 \underset{k_{b1}}{\overset{k_{f1}}{\rightleftarrows}} CaOH^+ + OH^-, \tag{3-1}$$

$$CaOH^+ \underset{k_{b2}}{\overset{k_{f2}}{\rightleftarrows}} Ca^{2+} + OH^-. \tag{3-2}$$

The values k_{f1}, k_{f2}, k_{b1}, and k_{b2} denote the rate constants of the forward and backward reactions, which follow the elementary reaction rate equation. The overall dissolution rate of calcium hydroxide particles is expressed as [34]

$$r_{dissolution} = A \cdot (-k_{f1} + k_{b1} \cdot [CaOH^+] \cdot f \cdot [OH^-] \cdot f), \tag{3-3}$$

where [·] denotes the molar concentration of the corresponding species, A is the total surface area of the $Ca(OH)_2$ solid particles in water, and *f* is the activity coefficient. During the reaction, the shrinkage of the solid particles causes the overall dissolution rate of calcium hydroxide to decreases in proportion to the total surface area of the solid. The activity coefficient *f* is calculated from the ionic strength I, expressed as

$$\log_{10}(f) = (-0.5\sqrt{I})/(1 + 1.4\sqrt{I}), \tag{3-4}$$

$$I = 0.5 \sum c_i z_i^2, \tag{3-5}$$

where c_i and z_i denote the concentration and charge number of the corresponding ion species in the solution, respectively.

The solubility of calcium hydroxide is expressed as a function of the temperature and particle size [34], as

$$\beta(Ca(OH)_2)_s = \sqrt{K_{Ca(OH)_2}} = \sqrt{\frac{k_{f1}}{k_{b1}}} = \left(5.214 - 0.0124\,T(K)\right) \cdot \exp\left(\frac{0.0313}{d(\mu m)}\right), \quad (3\text{-}6)$$

$$\log_{10} K_{CaOH^+} = \log_{10} \frac{k_{f2}}{k_{b2}} = -1.299 + 260.388\left(\frac{1}{298.15} - \frac{1}{T(K)}\right), \quad (3\text{-}7)$$

where d is the diameter of the $Ca(OH)_2$ particles, T(K) is the temperature in Kelvin, $K_{Ca(OH)_2}$ is the solubility equilibrium constant of calcium hydroxide, and K_{CaOH^+} is the thermodynamic equilibrium constant of $CaOH^+$.

Although the operating conditions reported in the literature differ slightly from ours, the rate constant of the forward reaction k_{f1}[kmol/m5·h] was estimated via the following form:

$$k_{f1} = 0.558 \cdot \exp\left(-\frac{29700}{R}\left(\frac{1}{T(K)} - \frac{1}{298.15}\right)\right). \quad (3\text{-}8)$$

The rate constant of the forward reaction k_{f2}[m3/kmol·h] was set to 1.958·102 25 so that we could formulate the rate constants k_{f1} and k_{f2} corresponding to our conditions. However, the variation of these constants does not contribute to the results, and a similar study [35] has shown that k_{f2} does not significantly affect the reaction rate.

3.2.2 Mass transfer of CO_2 gas into the alkali solution

The equation,

$$CO_2(g) \rightarrow CO_2(aq), \quad (3\text{-}9)$$

describes the chemisorption of CO_2 into the aqueous calcium hydroxide solution; before this can proceed, the CO_2 gas must be absorbed physically to the liquid phase. The mass transfer rate of CO_2 is expressed as [36]

$$r_{mass\ transfer} = -k_l a E\left(H^{CO_2}\rho_G Y_{CO_2} - [CO_2(aq)]\right), \quad (3\text{-}10)$$

where k_l and E are the overall mass transfer coefficient and enhancement factor for the chemical reactions, respectively. H^{CO_2} is the Henry's constant of CO_2 for the electrolyte solutions, and ρ_G and Y_{CO_2} are the molar density and CO_2 molar composition of the gas phase, respectively. Here, a is the specific interfacial area of the gas phase; it is expressed as [37]

$$a = \frac{1}{3D}\left(\frac{gD^2\rho_m}{\sigma_m}\right)^{0.5}\left(\frac{gD^3}{{v_m}^2}\right)^{0.1}{\alpha_g}^{1.13}, \quad (3\text{-}11)$$

where D is the reactor diameter, g is the gravitational acceleration, σ_m is the surface tension of the mixture, and ρ_m is the molar density. v_m is the kinematic viscosity of the liquid; this is estimated as $v_m=\mu_m/\rho_m$, where μ_m is the dynamic viscosity of the mixture, which is obtained from the modified Einstein equation [38]

$$\mu_m = \mu(1 + 2.5\emptyset + 14.1\emptyset^2), \quad (3\text{-}12)$$

where $\emptyset$ is the solid weight fraction in the solution. The gas holdup α_g is estimated using the following empirical equation [39]:

$$\alpha_g = 0.505{U_G}^{0.47}\left(\frac{0.072}{\sigma_m}\right)^{\frac{2}{3}}\left(\frac{0.0001}{\mu_m}\right)^{0.05}. \quad (3\text{-}13)$$

Here, U_G is the superficial gas velocity.

The overall mass transfer coefficient k_l is estimated from the Sherwood reaction of Brauer [40]:

$$\mathrm{Sh} = \frac{k_l d_b}{D_{CO_2}} = 2 + 0.015\mathrm{Re}^{0.89}\mathrm{Sc}^{0.7}. \quad (3\text{-}14)$$

Here, D_{CO_2} is the diffusivity of CO_2 in an aqueous electrolyte solution, obtained from the Aspen properties; Re and Sc denote the Reynolds and Schmidt numbers, respectively. d_b is the bubble diameter, calculated as $d_b=6\alpha_g/a$.

The enhancement factor E is calculated from the correlation [41]

$$E = \begin{cases} -\frac{Ha^2}{2(E_\infty - 1)} + \sqrt{\frac{Ha^4}{4(E_\infty - 1)^2} + \frac{E_\infty Ha^2}{E_\infty - 1} + 1} & E_\infty > 1, \\ 1 & E_\infty \le 1 \end{cases} \quad (3\text{-}15)$$

where

$$E_\infty = \left(1 + \frac{[OH^-]D_{OH^-}}{2D_{CO_2}H^{CO_2}\rho_G Y_{CO_2}}\right) \times \sqrt{\frac{D_{CO_2}}{D_{OH^-}}}, \quad (3\text{-}16)$$

$$Ha = \frac{\sqrt{k_{11}D_{CO_2}[OH^-]}}{k_l}. \quad (3\text{-}17)$$

D_{OH^-} is the diffusivity of OH^- in the aqueous electrolyte solution, also available in the Aspen properties; k_{11} is the rate constant of the reaction between $CO_2(aq)$ and $OH^-(aq)$, which is discussed in the next section.

The Henry's constant of CO2 for the electrolyte solution H^(CO_2) is determined from [42]

$$\log\left(\frac{H^{w}}{H^{CO_2}}\right) = \sum\left(h_i + h_g\right)c_i, \tag{3-18}$$

where c_i is the concentration of the corresponding ion species in the solution, and h_i and h_g are the ion- and gas-specific parameters, respectively. H^w is the solubility coefficient of CO_2 in pure water, which is obtained from the following equation [43]:

$$H^{w} = 3.59E^{-7}RTe^{\frac{2044}{T(K)}}. \tag{3-19}$$

3.2.3 Ionic reactions and precipitation of calcium carbonate

The equations,

$$CO_2(aq) + OH^- \underset{k_{12}}{\overset{k_{11}}{\rightleftarrows}} HCO_3^-, \tag{3-20}$$

$$HCO_3^- + OH^- \underset{k_{22}}{\overset{k_{21}}{\rightleftarrows}} CO_3^{2-} + H_2O, \tag{3-21}$$

$$OH^- + H^+ \underset{k_{32}}{\overset{k_{31}}{\rightleftarrows}} H_2O, \tag{3-22}$$

$$CO_2(aq) + H_2O \underset{k_{42}}{\overset{k_{41}}{\rightleftarrows}} HCO_3^- + H^+, \tag{3-23}$$

$$Ca^{2+} + CO_3^{2-} \underset{k_{52}}{\overset{k_{51}}{\rightleftarrows}} CaCO_3, \tag{3-24}$$

$$CaCO_3 + H^+ \underset{k_{62}}{\overset{k_{61}}{\rightleftarrows}} Ca^{2+} + HCO_3^-, \tag{3-25}$$

describe the chemisorption of CO_2 in an acid-base equilibrium [Eqs. (20)–(23)] and the precipitation of calcium carbonate [Eqs. (24)-(25)]. The reaction rate constants and equilibrium constants used in Eqs. (20)–(25) are summarized in Table #, where ρ_w is the density of water (kg m^{-3}).

Table 10 Kinetic parameters used for the ionic reactions and precipitation of calcium carbonate

	Definition	Unit	Reference
k_{11}	$10^{11.916-\frac{2382}{T(K)}}$	$\frac{L}{mol \cdot s}$	44
k_{12}	$\frac{k_{11}K_w}{K_1}$	$\frac{1}{s}$	
K_1	$\exp\left(-\frac{12092.1}{T(K)} - 36.786\ln(T(K)) + 235.482\right) \cdot \rho_w$	$\frac{kmol}{m^3}$	45
k_{21}	6×10^6	$\frac{m^3}{mol \cdot s}$	46
k_{22}	$\frac{k_{21}}{K_2}$	$\frac{1}{s}$	
K_2	$10^{\frac{1568.9}{T(K)}-2.5866-6.737\times10^{-3}T(K)}$	$\frac{m^3}{mol}$	47
k_{31}	1.4×10^{14}	$\frac{L}{mol \cdot s}$	46
k_{32}	$\frac{k_{31}}{K_w}$	$\frac{mol}{L \cdot s}$	
K_w	$10^{-\frac{5839.5}{T(K)}-22.4773\log(T(K))+61.2062} \cdot \rho_w^2$	$\frac{mol^2}{L^2}$	48
k_{41}	2.4×10^{-2}	$\frac{1}{s}$	49
k_{42}	$\frac{k_{41}}{K_1}$	$\frac{L}{mol \cdot s}$	
k_{51}	$\frac{k_{52}}{K_{CaCO_3}}$	$\frac{L}{mol \cdot s}$	50
k_{52}	9×10^{-3}	$\frac{mol}{L \cdot s}$	51
K_{CaCO_3}	$10^{-171.9065-0.077993\,T(K)+\frac{2839.319}{T(K)}+71.595\log_{10}T(K)}$	$\frac{mol^2}{L^2}$	50
k_{61}	10^6	$\frac{L}{mol \cdot s}$	51
k_{62}	4×10^2	$\frac{1}{s}$	51

3.3 Process design and modeling

The reactor model involves a set of differential algebraic equations (DAEs) that describe the reaction kinetics (aforementioned), phase equilibrium, and heat and material balances, amongst others. The Pitzer model was chosen as the thermodynamic property package in ACM, because it has been successfully applied to predict the solubility of salts and $Ca(OH)_2$ in alkali systems [52]. This model describes the physical characteristics (e.g., the density, diffusivity, viscosity, and heat capacity) as a function of the temperature and pressure of each component, to estimate the reactions, mixing, and vaporization heats. In this section, we introduce the MC process formulation, as well as its underlying assumptions.

3.3.1 Assumptions

- Gas bubbles, solids, and ions are uniformly distributed throughout the reactor (i.e., well-mixed conditions).
- We possess only information regarding the CO_2 and H_2O contents of the flue gas from the operation: the gas contains 15 vol% CO_2, with the remaining volume being air containing N_2 and O_2 in a molar ratio of 79:21. Subsequently, H_2O is added to make up 20 vol% of the total flue gas.
- No pressure drop occurs in the reactor; that is, the pressure of the process is held constant at 1 atm.
- In the DAEs of the reaction kinetics, the volume of the liquid phase is assumed to be constant, owing to the incompressibility of the fluid.

- The $Ca(OH)_2$ particles shrink as the reaction proceeds, and the number of solid particles remains constant until the reactants are replenished.

3.3.2 Reactor modelling

The equations,

$$\frac{dn_{CO_2(g)}}{dt} = -k_l aE\left(H^{CO_2}\rho_G Y_{CO_2} - [CO_2(aq)]\right), \tag{3-26}$$

$$\frac{1}{V}\frac{dn_{Ca(OH)_2(s)}}{dt} = -A(k_{f1} - k_{b1}[CaOH^+]f[OH^-]f), \tag{3-27}$$

$$\frac{1}{V}\frac{dn_{Ca^{2+}}}{dt} = k_{f2}[CaOH^+]f - \frac{k_{f2}}{K_{CaOH^+}}[Ca^{2+}]f^4[OH^-]f - k_{51}[Ca^{2+}][CO_3^{2-}] + k_{52} + k_{61}[H^+] - k_{62}[Ca^{2+}][HCO_3^-], \tag{3-28}$$

$$\frac{1}{V}\frac{dn_{CaCO_3(s)}}{dt} = k_{51}[Ca^{2+}][CO_3^{2-}] - k_{52} - k_{61}[H^+] + k_{62}[Ca^{2+}][HCO_3^-], \tag{3-29}$$

$$\frac{1}{V}\frac{dn_{CaOH^+}}{dt} = A(k_{f1} - k_{b1}[CaOH^+]f[OH^-]f) - \left(k_{f2}[CaOH^+]f - \frac{k_{f2}}{K_{CaOH^+}}[Ca^{2+}]f^4[OH^-]f\right), \tag{3-30}$$

$$\frac{1}{V}\frac{dn_{CO_2(aq)}}{dt} = -k_{11}[CO_2(aq)][OH^-] + k_{12}[HCO_3^-] - k_{41}[CO_2(aq)] + k_{42}[HCO_3^-][H^+], \tag{3-31}$$

$$\frac{1}{V}\frac{dn_{CO_3^{2-}}}{dt} = k_{21}[HCO_3^-][OH^-] - k_{22}[CO_3^{2-}] - k_{51}[Ca^{2+}][CO_3^{2-}] + k_{52}, \tag{3-32}$$

$$\frac{1}{V}\frac{dn_{H_2O}}{dt} = k_{21}[HCO_3^-][OH^-] - k_{22}[CO_3^{2-}] + k_{31}[OH^-][H^+] - k_{32} - k_{41}[CO_2(aq)] + k_{42}[HCO_3^-][H^+], \tag{3-33}$$

$$\frac{1}{V}\frac{dn_{H^+}}{dt} = -k_{31}[OH^-][H^+] + k_{32} + k_{41}[CO_2(aq)] - k_{42}[HCO_3^-][H^+] - k_{61}[H^+] + k_{62}[Ca^{2+}][HCO_3^-], \quad (3\text{-}34)$$

$$\frac{1}{V}\frac{dn_{HCO_3^-}}{dt} = k_{11}[CO_2(aq)][OH^-] - k_{12}[HCO_3^-] - k_{21}[HCO_3^-][OH^-] + k_{22}[CO_3^{2-}] + k_{41}[CO_2(aq)] - k_{42}[HCO_3^-][H^+] + k_{61}[H^+] - k_{62}[Ca^{2+}][HCO_3^-], \quad (3\text{-}35)$$

$$\frac{1}{V}\frac{dn_{OH^-}}{dt} = -k_{11}[CO_2(aq)][OH^-] + k_{12}[HCO_3^-] - k_{21}[HCO_3^-][OH^-] + k_{22}[CO_3^{2-}] - k_{31}[OH^-][H^+] + k_{32} + A(k_{f1} - k_{b1}[CaOH^+]f[OH^-]f) + k_{f2}[CaOH^+] - \frac{k_{f2}}{K_{CaOH^+}}[Ca^{2+}]f^4[OH^-]f, \quad (3\text{-}36)$$

are the reaction kinetic equations, where V and n are the volume and the number of moles of the liquid–solid mixture and gas phase in the reactor, respectively.

The total surface area A of the $Ca(OH)_2$ particles was calculated as follows: we multiplied the number of $Ca(OH)_2$ particles by the volume of one $Ca(OH)_2$ particle, to obtain the total volume of $Ca(OH)_2$ particles, as

$$n_p \cdot \frac{4}{3}\pi\left(\frac{d}{2}\right)^3 = \frac{S \cdot x}{\rho_m}, \quad (3\text{-}37)$$

where n_p is the number of $Ca(OH)_2$ particles; x and ρ_m are the mole fraction and molar density of $Ca(OH)_2$, respectively; and S is the number of $Ca(OH)_2$ per mole. From this, we could calculate the total surface area of $Ca(OH)_2$ particles using

$$A = n_p \pi d^2 = \frac{6 \cdot S \cdot x}{\rho_m \cdot d}. \quad (3\text{-}38)$$

3.3.3 Sequence of reactant replenishment

Figure 12 presents the process flow diagram of the aqueous MC process. The reactor comprises a flat-bottomed stirred tank of height 4 m and diameter 4 m. The reactant solution was filled into the reactor according to a replacement cycle; meanwhile, the flue gas was continuously outputted from the power plant and bubbled through the gas sparger in the reactor. Thus, this process is a semi-continuous process in which reactants and product are repeatedly added and removed during operation, respectively.

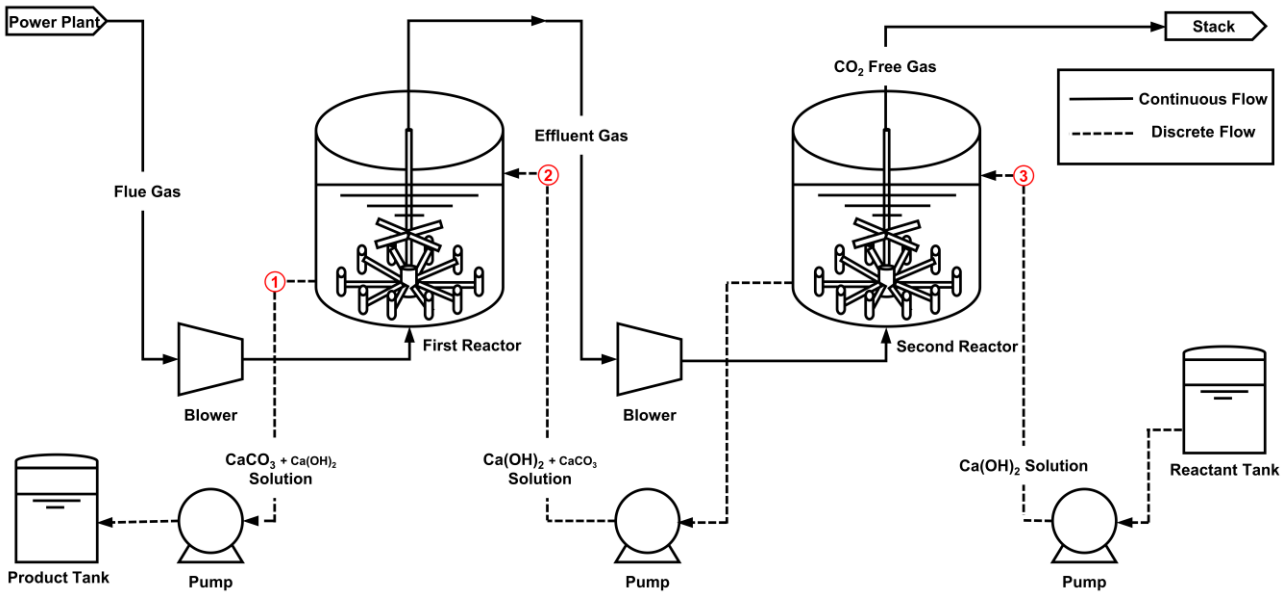

Figure 12 Process flow diagram of the aqueous MC process.

The condition of a 20 wt% $Ca(OH)_2$ solution means that the concentration is supersaturated. During operation, the pH value of the liquid phase was almost constant, whereas the pH value and CO_2 removal efficiency were drastically decreased when the reactants were entirely depleted. Because the number of $Ca(OH)_2$ solid particles in the reactor is not measurable, the time point for replenishment cannot be predicted. Therefore, the process must be operated according to the specified operation recipe, which comprises a sequence of tasks. The circled numbers in Figure 12 denote the corresponding steps of the operation recipe Case 1 summarized in Table 11. Defining the replenishment quantity required over time is the most important step to satisfying the CO_2 removal efficiency requirement (of 90% or above) during operation. The operation recipe Case 1 (referred to as the Base Case) is summarized in Table 11 with respect to the pilot-plant operation.

Table 11 Sequence of operation recipe Case 1 (Base Case)

Base Case
Reactants are replenished sequentially when the reactants of the first reactor are depleted. 1. Remove the product solution from the first reactor. 2. Shift the reactant solution from the second to the first reactor. 3. Replenish the reactant in the second reactor.

3.3.4 ACM model validation

The dynamic simulation results (e.g., the pH and temperature of each reactor and the overall CO_2 removal efficiency) were compared with actual pilot-plant operation data. Figure 13(a) and 13(b) depict the batch operation, to which no additional reactants were added; the concentrations of the $Ca(OH)_2$ solution were 15 wt% and 20 wt%, respectively. Figure 13(c) shows the semi-continuous operation, in which the reactants were replenished six times. In Figure 13, Eff. indicates the overall CO_2 removal efficiency, (Exp.) and (Sim.) denote the pilot-plant operation data and the dynamic simulation result, respectively, and pH_i and T_i are the pH value and temperature in the i-th reactor, respectively.

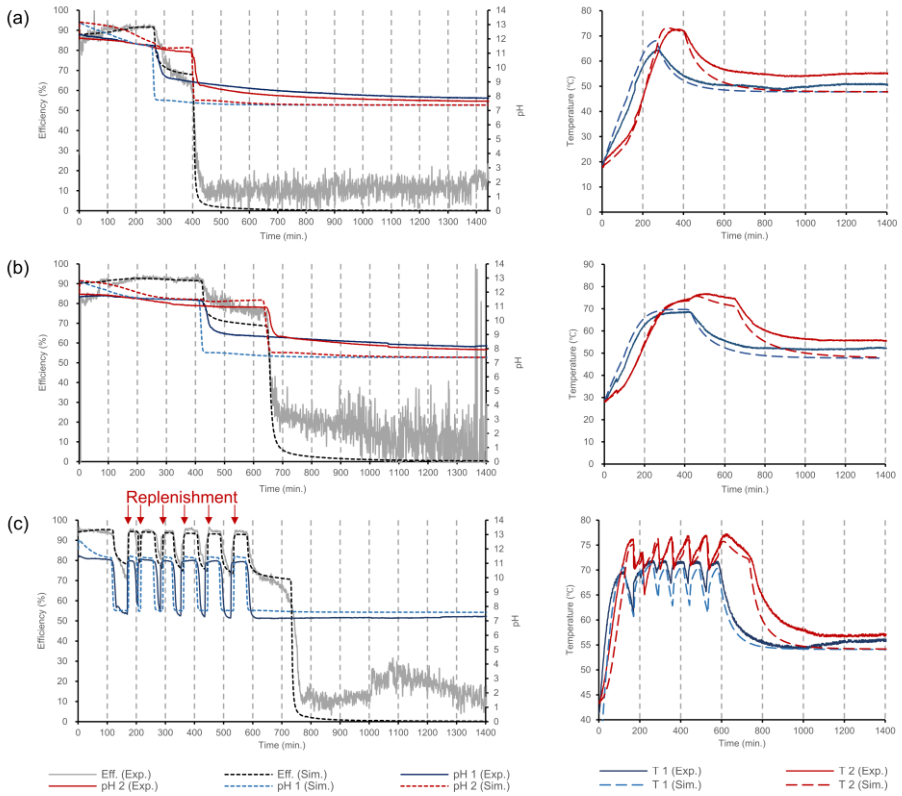

Figure 13 Comparison between the simulation results and pilot-plant operation data: (a) batch operation with 15 wt% $Ca(OH)_2$ solution, (b) batch operation with 20 wt% $Ca(OH)_2$ solution, and (c) semi-continuous operation with 20 wt% $Ca(OH)_2$ solution.

3.4 Summary

Because the reactants in the first reactor were entirely depleted before those in the second reactor, the overall CO_2 removal efficiency decreased via two stages. CO_2 removal took place after the reactants in both reactors were depleted, owing to the unreacted reactant. It may be thought that this is because $CaCO_3$ can grow on the surface of the $Ca(OH)_2$ particles, and the solid particles can stagnate without contacting the liquid phase below the gas sparger, causing the $Ca(OH)_2$ dissolution to interfere. At present, several questions remain unanswered, and we decided to neglect the occurrence of CO2 removal after the reaction was terminated.

In this study, only the reaction end time was estimated (other reaction kinetic parameters were neglected); this was performed by determining the quantity of unreacted reactant, because we were focusing on the operation recipe. In other words, the main purpose of the modeling is to find out when the reaction ends and to ensure that the overall CO_2 removal efficiency exceeds 90% during operation. Consequently, we concluded that the model is acceptable for the operation recipe optimization in that the mean absolute percentage error of the overall CO2 removal efficiency in Figure 2(c) was ~3.7% (~9 h after the start of replenishment).

Chapter 4

Bayesian optimization approach to semi-continuous carbonation process operation recipe

4.1 Introduction

An aqueous MC process, which was modeled in the previous chapter, is operated semi-continuously. In the semi-continuous process, the reactants and products are repeatedly replenished and removed, respectively, according to the operation recipe. The key for optimizing the operation recipe in the semi-continuous process is to replenish the mineral solution when the reactants are completely consumed; this maintains the CO_2 removal efficiency at the desired value. However, previous studies into operation recipes have only considered parameters (e.g., temperature, pressure, concentration, and reaction time) for batch process recipes, to investigate reaction kinetics or product morphologies. Moreover, companies' specific operation recipes are confidential, and the operation recipe (used in actual pilot-plant operations) has poor improvement potential owing to its simplicity. Thus, in this study, we propose an optimized operation recipe for the semi-continuous process, to improve the existing operation recipes of an actual pilot plant that captures 40 tons of CO_2 per day using a 20 wt% aqueous $Ca(OH)_2$ solution with a power-plant-generated flue gas containing 15 vol% CO_2.

Recipe optimizations are a type of hyperparameter optimization problem in which the replenishment sequence is determined beforehand. In addition, because this process model must be dynamically simulated (to monitor reaction dynamics), a long simulation time is required to ensure that the constraints are satisfied during the entire operation (i.e., from startup to steady state). Hence, Bayesian optimization is adopted to optimize the semi-continuous carbonation process recipe. In addition, two new operation recipes are proposed: a sequence including both a continuous and discrete flow and one involving additional reactant replenishment.

In this chapter, the operation recipe optimization procedure for the aqueous MC process is described. The main objective of our study was to maintain an overall CO_2 removal efficiency, which is estimated the CO_2 content ratio between the in- and out- flow of the aqueous MC process, of at least 90% and to minimize the quantity of reactant used. However, the operation recipe (Case1: Base case) described in the previous chapter has poor potential for improvement, owing to its simplicity; furthermore, a long dynamic simulation time is required to ensure that the efficiency exceeds 90% during the reactant replenishment sequence; hence, numerous iterations are required for the model to converge the nonlinear solver, because the mass and energy change rapidly.

If solely the quantity of reactant replenished in the Case 1 recipe is used as an objective function, a liquid level fraction and smaller replenishment quantity will achieve optimal results. Hence, the optimal procedure would be to continuously replenish a small amount of reactant. Moreover, several companies prefer semi-continuous operations, to minimize the quantities of

unreacted reactants by preventing short-circuit flow (i.e., when the product reaches the outlet before the residence time has elapsed).

4.2 Problem descriptions

When optimizing the Case 1 operation recipe with a single objective function, the replenishment period was less than 3 min and the pumps were turned on/off too frequently, resulting in damage. Therefore, the replenishment period is used as another objective function. the multi-objective optimization problem is solved to minimize the quantity of reactant used and maximize the replenishment period for four optimization variables: the lower and upper limits of the liquid level fraction of the first reactor, LLF1min and LLF1max, respectively; and the lower and upper limit of the liquid level fraction of the second reactor, LLF2min and LLF2max, respectively. Thus, in terms of the operation sequence, the reactants were removed from the first reactor until its liquid level fraction reached LLF1min; then, the reactants were shifted from the second to the first reactor until the first reactor's liquid level fraction reached LLF1max. Finally, the reactants were replenished in the second reactor until its liquid-level fraction reached LLF2max. At the end of each operation step, all flow rates of the reactant stream were zero. The minimum and maximum values of these optimization variables were set to 0.5 and 0.8, respectively, considering the operational limitations imposed by the impeller position and overflow. Subsequently, the optimization variables were discretized in elements of 0.01. However, because the liquid level of the first reactor decreased first during replenishment, the overall CO_2 removal efficiency was below 90% when the liquid levels in both reactors were low. Hence, maintaining high liquid levels in both reactors was preferable. Therefore, to reduce the computational load,

we decided to remove LLF2min and set the optimization variable minimum to 0.65. Thus, the liquid level fraction of the second reactor remained above 0.5, and the number of combinations decreased from 6,580 to 1,920. The flow rate of the liquid stream was set as that described in the pilot-plant operation data.

The Case 2 (the so-called “Continuous Case”) operation recipe was proposed to include both continuous and discrete replenishment sequences, to assess whether a smaller instantaneous replenishment quantity was preferable. In addition, the flow rate of the continuous flow was set much smaller than that of the discrete flows, to prevent short-circuit flow. Table 12 shows the sequence for the Continuous Case. This case differs from the Base Case in that all flow rates of the replenishment stream were non-zero at the end of each operation step. Therefore, the flow rate Fc of the continuous replenishment stream was included as another optimization variable, which was set within the range 0–600 kmol/h and discretized in steps of 10 kmol/h. When Fc was zero, this optimization problem matched that of the Base Case.

Table 12 Operation sequence for Case 2 (Continuous Case)

Continuous Case
Reactants are replenished sequentially and flow slightly continuously.
1. Remove the product solution from the first reactor.
2. Shift the reactant solution from the second to the first reactor.
3. Replenish the reactant in the second reactor.
4. Maintain the flow rate of all replenishment streams at their specified values.

The Case 3 (the so-called “Buffer Case”) operation recipe was proposed to include a sequence of adding supplementary reactants. By adding the reactants as a buffer before replenishment, the overall CO_2 removal efficiency was maintained above 90%, even when the replenishment quantity was increased relative to the Base Case. This case differs from the Base Case in that the second and third steps of the operation sequence of the Base Case were executed before replenishment. Therefore, the optimization problem is solved for five optimization variables: the lower limit of the liquid level fraction of the first reactor, LLF1min; the upper limit of the buffer liquid level fraction of the first reactor, LLF1max1; the upper limit of the liquid level fraction of the first reactor, LLF1max2; the upper limit of the buffer liquid level fraction of the second reactor, LLF2max1; and the upper limit of the liquid level fraction of the second reactor, LLF2max2. Table 13 shows the operation sequence for the Buffer Case; here, the reactants are shifted from the second to the first reactor until the liquid level fraction of the first reactor reaches LLF1max1. Subsequently, the reactants are replenished to the second reactor until its liquid level fraction reaches LLF2max1. Then, the operation proceeds according to Steps 1–3 of the Base Case. At the end of each operation step, all flow rates of the reactant stream are likewise zero.

Table 13 Operation sequence for Case 3 (Buffer Case)

Buffer Case
Reactants are added first as a buffer and replenished sequentially.
1. Shift the reactant solution from the second to the first reactor
2. Replenish the reactant solution in the second reactor.
3. Remove the product solution from the first reactor.
4. Shift the reactant solution from the second to the first reactor.
5. Replenish the reactant solution in the second reactor.

Table 14 presents the mathematical formulations for each case. The purpose of solving the three multi-objective optimization problems is to identify the set of all non-dominated optimization variables $x \in X$, referred to as the Pareto set. The objective functions f_1 and f_2 were extracted from the ACM dynamic simulation, which was run for 20 hours because the maximum time required to achieve a steady state from the startup conditions was below 20 hours. Function f_2 (i.e., Nr) was inversely proportional to the replenishment period (i.e., the replenishment period Pr, = 20 h/Nr). It took ~1–2 hours real-time to simulate one 20 hours ACM dynamic simulation run using eight CPU cores of Intel® Xeon® CPU E5-1680 v4 @ 3.4GHz. Because it is difficult to locate the Pareto front analytically in most practical applications, the continuous-space optimization variables were discretized for all cases, to reduce computational time. X denotes the search domain, where each point represents a different replenishment quantity; the domain comprises a discrete space of three dimensions ($\mathcal{D}^3$) for the Base Case. The optimization variable vector x for this case is composed of three optimization variables (v_1, v_2, v_3); each variable takes 16 values with a regular grid spacing. Hence, the optimization space in the Base Case features 16^3 = 4,096 grid points. However, because v_1 (LLF1min) must be lower than v_2 (LLF1max), the number of optimization variables combinations is reduced to 1,920. When $v_1 = v_2$, no replenishment occurs. For the Buffer Case, the number of optimization variable combinations is reduced from 16^5 = 1,048,576 to 143,360, because of the following constraints: v_1 (LLF1min) must be lower than v_3 (LLF1max2); and v_2 must exceed v_3 (LLF1max2). If v_4 (LLF2max) is lower than v_5 (LLF2max2) minus ($v_2 - v_3$), then the second step in the operation sequence of the Buffer Case is neglected.

It is important to prevent reactant depletion in the first reactor, and the reactant in the second reactor is never depleted; hence, the second step in the operation sequence of the Buffer Case is negligible.

Table 14 Summary of multi-objective operation recipe optimizations for each case

	Base Case	Continuous Case	Buffer Case
Objective functions	$\min(f_1(x), f_2(x))$ where $f_1(x)$ = the amount of reactant used [Lt(x)] and $f_2(x)$ = the number of replenishment [Nr(x)].		
Optimization variables	$x = [v_1, v_2, v_3] \in X$, $X = \{x=[v_1, v_2, v_3] \mid x \in \mathcal{D}^3$, $v_1 \in \{0.65, 0.66, \ldots, 0.80\}$, $v_2 \in \{0.65, 0.66, \ldots, 0.80\}$, $v_3 \in \{0.65, 0.66, \ldots, 0.80\}\}$ where, v_1 = LLF1min, v_2 = LLF1max, v_3 = LLF2max.	$x = [v_1, v_2, v_3, v_4] \in X$, $X = \{x=[v_1, v_2, v_3, v_4] \mid x \in \mathcal{D}^4$, $v_1 \in \{0.65, 0.66, \ldots, 0.80\}$, $v_2 \in \{0.65, 0.66, \ldots, 0.80\}$, $v_3 \in \{0.65, 0.66, \ldots, 0.80\}$, $v_4 \in \{0, 10, \ldots, 600\}\}$ where, v_1 = LLF1min, v_2 = LLF1max, v_3 = LLF2max, v_4 = Fc.	$x = [v_1, v_2, v_3, v_4, v_5] \in X$, $X = \{x=[v_1, v_2, v_3, v_4, v_5] \mid x \in \mathcal{D}^5$, $v_1 \in \{0.65, 0.66, \ldots, 0.80\}$, $v_2 \in \{0.65, 0.66, \ldots, 0.80\}$, $v_3 \in \{0.65, 0.66, \ldots, 0.80\}$, $v_4 \in \{0.65, 0.66, \ldots, 0.80\}$, $v_5 \in \{0.65, 0.66, \ldots, 0.80\}\}$ where, v_1 = LLF1min, v_2 = LLF1max1, v_3 = LLF1max2, v_4 = LLF2max1, v_5 = LLF2max2.
Constraints	Eff. $\geq$ 90, $v_1 < v_2$	Eff. $\geq$ 90, $v_1 < v_2$	Eff. $\geq$ 90, $v_1 < v_3 < v_2$
	where Eff. is the overall CO_2 removal efficiency [%].		
Number of combinations	1,920	117,120	143,360

4.3 Multi-objective Bayesian optimization algorithm

Bayesian optimization is an effective framework for the global optimization of an objective function that is expensive to evaluate (e.g., a block-box function with an unknown structure and a function whose derivative form is unknown). In the Bayesian optimization algorithm, the objective function is evaluated sequentially and iteratively via a stochastic interpolation method [referred to as kriging or Gaussian process (GP) regression] and Bayes' theorem, which states that the posterior probability is proportional to the likelihood probability multiplied by the prior probability. In this study, the ACM model described in the previous section was used as a black-box function for Bayesian optimization. Table 15 shows the general Bayesian optimization algorithm [53], where u(x) is the acquisition function, f(x) is the real (or black-box) function to be optimized, yn is the objective function, ε is the measurement noise, and $\mathcal{D}_{1:n}$ is the set of observation data for Iterations 1–n. The algorithm was repeated until the stopping criterion was satisfied.

Table 15 General procedure of Bayesian optimization algorithm

Algorithm Bayesian Optimization
for $n = 1, 2, \ldots$ **do**
Find x_n by maximizing the acquisition function over the GP : $x_n = \text{argmax}_x u(x\|\mathcal{D}_{1:n-1})$.
Evaluate the objective function with x_n : $y_n = f(x_n) + \varepsilon_n$.
Augment the data $\mathcal{D}_{1:n} = \{\mathcal{D}_{1:n-1},(x_n, y_n)\}$ and update the GP.
if the stopping criterion is met **then**
break
end if
end for

The GP is a stochastic process that predicts, from the observation data, the function values for an unexplored point, using the principle that every finite linear combination of function values is a multivariate normal distribution. Hence, any objective function value $f(x_1)$, $f(x_2)$, ..., $f(x_n)$ at some finite point x_1, x_2, ..., x_n follows the multivariate Gaussian distribution with a mean function m and covariance function K, as

$$f(x_{1:n}) \sim N\left(m(x_{1:n}), \mathbf{K}(x_{1:n}, x_{1:n})\right), \tag{4-1}$$

where $x_{1:n}$ denotes x_1, x_2, ..., x_n, $f(x_{1:n}) = [f(x_1), f(x_2), ..., f(x_n)]$, $m(x_{1:n}) = [m(x_1), m(x_2), ..., m(x_n)]$, and $K(x_{1:n}, x_{1:n}) = [k(x_1, x_1), ..., k(x_1, x_n); ...; k(x_n, x_1), ..., k(x_n, x_n)]$. For convenience, the mean function is set to a constant value, typically zero. Thus, the covariance function represents the behaviors of the objective function (e.g., stationarity, smoothness, isotropy, and periodicity). One of the most common covariance functions is the isotropic Matérn 5/2 kernel, which we employ in this study. It is expressed as

$$k_{M52}(x, x') = \theta_0 \left(1 + \sqrt{5r^2(x, x')} + \frac{5}{3} r^2(x, x')\right) \exp\left\{-\sqrt{5r^2(x, x')}\right\}, \tag{4-2}$$

where θ_0 is the covariance amplitude, $r^2(x,x') = (x-x')^T \Lambda (x-x')$, and Λ is the diagonal matrix of d-squared length scales $\theta_{1:d}$. A short distance between two points [i.e., a small $r^2(x,x')$ value] implies a large mutual influence. The covariance amplitude and length scale are hyperparameters that define the behavior of the objective function. In this study, these hyperparameters were estimated from observations, using the restricted maximum likelihood (ReML) method. Subsequently, the function value $f(x_{n+1})$ at the candidate for the next

evaluation point x_{n+1} was predicted using the fact that $f(x_{1:n})$ and $f(x_{n+1})$ are both Gaussian distributions, expressed as

$$\begin{bmatrix} f(x_{1:n}) \\ f(x_{n+1}) \end{bmatrix} \sim N\left(0, \begin{bmatrix} \mathbf{K} & k \\ k^{T} & k(x_{n+1}, x_{n+1}) \end{bmatrix}\right), \tag{4-3}$$

where $k = [k(x_{n+1}, x_1), k(x_{n+1}, x_2), ..., k(x_{n+1}, x_n)]$. The predictive posterior probability distribution of $f(x_{n+1})$ can be expressed using Bayes' theorem, as

$$P(f(x_{n+1})|\mathcal{D}_{1:n}, x_{n+1}) = N\left(\mu_n(x_{n+1}), \sigma^2{}_n(x_{n+1})\right), \tag{4-4}$$

where $\mu_n(x_{n+1}) = k^T K^{-1} f(x_{1:n})$ and $\sigma^2{}_n(x_{n+1}) = k(x_{n+1}, x_{n+1}) - k^T K^{-1} k$. With this predictive posterior probability distribution, the point to be evaluated is determined by maximizing the acquisition function, which guides the search for the optimum. In this study, to solve the multi-objective optimization problem, we adopted the expected maximin improvement u_{EMMI} [54] as an acquisition function; this represents an extension of the expected improvement u_{EI} [55] (an acquisition function) employed for single objective optimization problems; it evaluates the expected value of the improvement function I. The formulations of u_{EI} and I are given by

$$I\left(f(x_{n+1})\right) = \left(\min\left(f(x_{1:n})\right) - f(x_{n+1})\right) \cdot 1_{[\min(f(x_{1:n})) > f(x_{n+1})]}, \tag{4-5}$$

$$\begin{aligned} u_{EI}(x) &= \mathbf{E}\left[I\left(f(x_{n+1})\right)\right] \\ &= \left[\left(\min\left(f(x_{1:n})\right) - \mu_n(x_{n+1})\right)\Phi\left(\frac{\left(\min\left(f(x_{1:n})\right) - \mu_n(x_{n+1})\right)}{\sigma_n(x_{n+1})}\right)\right. \\ &\quad \left. + \sigma_n(x_{n+1})\phi\left(\frac{\left(\min\left(f(x_{1:n})\right) - \mu_n(x_{n+1})\right)}{\sigma_n(x_{n+1})}\right)\right] \cdot 1_{[\sigma_n(x_{n+1})>0]}, \end{aligned} \tag{4-6}$$

where $1_{[E]}$ is 1 if E is true and zero if E is false, E[·] is the expected value, Φ(·) is the standard normal cumulative distribution function, and ϕ(·) is the corresponding density function. u_{EI} is large when the value of the improvement function is large, or when a new observation $f(x_{n+1})$ has considerable uncertainty. Similar to u_{EI}, u_{EMMI} is approximated using the maximin improvement function I_M, expressed as

$$I_M\left(f(x_{n+1})\right) = -\max_{x_i \in p_x} \min_{j=1,2,\dots} \left(f_j(x_{n+1}) - f_j(x_i)\right) \cdot 1_{\left[-\max_{x_i \in P_x} \min_{j=1,2,\dots} \left(\min\left(f_j(x_{n+1})\right) - f_j(x_i)\right) > 0\right]}, \quad (4\text{-}7)$$

where p_x is the set of x inputs correlated with the set of nondominated outputs up to that point (i.e., the x input set of the current Pareto front) and j represents each objective function. Hence, if max(j) = 1, I_M = I. IM indicates the extent to which a new observation $f_j(x_{n+1})$ will improve the current Pareto front. Because this is difficult to formulate in a closed-form expression, u_{EMMI} is computed approximately using Monte Carlo simulations.

The flow chart in Figure 14 shows the algorithm of an optimizer for the multi-objective Bayesian optimization algorithm, developed in MATLAB using the open toolbox STK v. 2.5.1 [56]. First, the optimizer searches for an initial set using a regular grid-sampling method for each case. Here, the numbers of initial sets for Cases 1, 2, and 3 were 18, 126, and 90, respectively. Then, the hyperparameters of two GPs for each objective function (with zero mean function and isotropic Matérn 5/2 kernel) were estimated at every fifth iteration to fit the cumulative observation data as the algorithm progressed, using the ReML method. With these properties, the GP regression generated a

posterior probability distribution displaying the mean and variance of the objective function values for every candidate in the input domain.

Using the posterior probability distribution, the acquisition function u_{EMMI} was approximated by averaging over 20,000 random samples of the objective function, using the Monte Carlo method. In other words, the acquisition function value was estimated by averaging 20,000 acquisition function values derived from 20,000 different hyperparameters of GP using observations. The next evaluation point xnext was then determined by locating the argument of the acquisition function maximized over x. To improve performance, the objective function values were normalized according to the initial observations; that is, $\max(y_j(x_{ini})) = 1$ and $\min(y_j(x_{ini})) = 0$, where x_{ini} is the set of initial training data. Subsequently, the ACM simulation was run with the new set x_{next} by linking MATLAB to ACM, using the Simulink model with the Aspen Modeler Block provided by Aspen Tech®. When the CO_2 removal efficiency fell below 90% during the simulation, the ACM simulation was terminated, and both objective values were set to the maximum value, to impose a penalty. The simulations were run for 20 hours without constraint violations; then, the results from the ACM were transferred to the optimizer in MATLAB, and the Pareto front was updated with the new observation dataset.

The stopping criterion for the algorithm was set by considering the computational budget and the Pareto front saturation. First, the minimum number of iterations was set to 0.25% of the number of optimization variable combinations. Then, the algorithm was terminated when the hypervolume of the dominated area—estimated using the Pareto front and maximum values of

each objective function—showed no increase for 25% of the number of iterations over which the dominated hypervolume was last increased. In Cases 1–3, the minimum numbers of iterations were 5, 293, and 356, respectively. We set a factor of 0.25% because the maximum value of expected improvement—the most common criterion for determining whether a Bayesian optimization algorithm is adequately implemented—was sufficiently small (below 0.15) after 200 and 260 iterations for Cases 2 and 3, respectively. Thus, we proposed a criterion that provided both qualitative and quantitative information for the algorithm termination, accounting for the dominated hypervolume. However, increasing the number of iterations increases the dominated hypervolume and decreases the maximum value of expected improvement; expressed otherwise, it achieves a more accurate Pareto front. As a user-inputted parameter, the stopping criteria can be adjusted according to the computational resources.

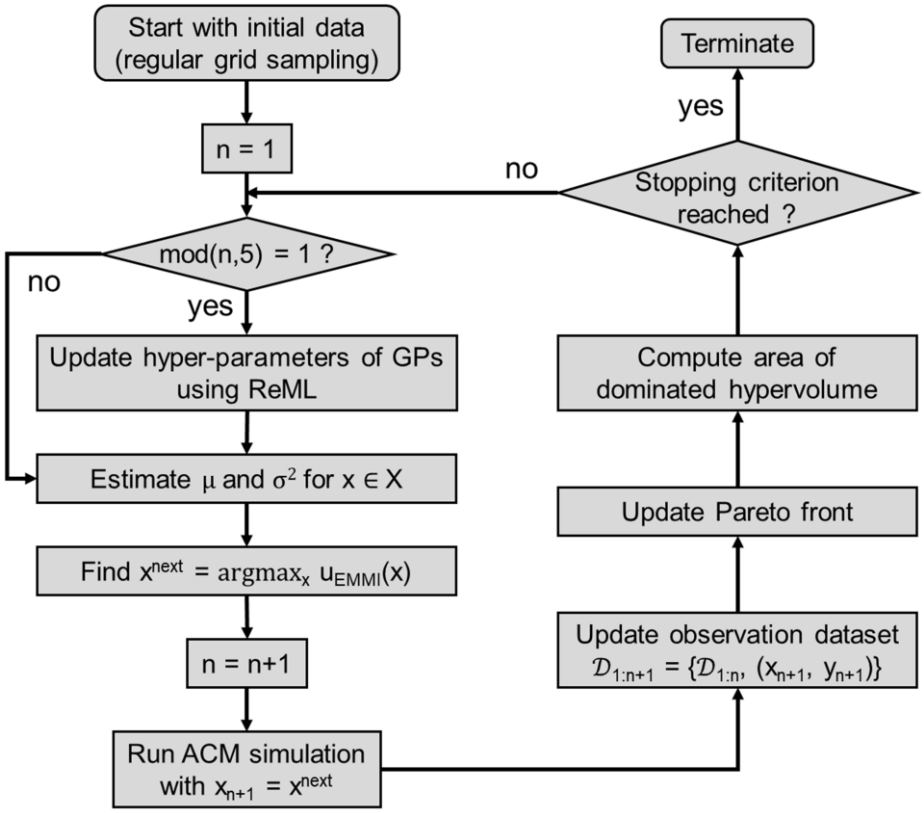

Figure 14 Multi-objective Bayesian optimization algorithm for the operation recipes.

4.4 Results and discussion

Figure 15 shows the results of the multi-objective Bayesian optimization for the Base Case. The objective function values can exceed between 0 and 1 during iteration, because the normalization is based upon initial observations alone. When the values are normalized by the updated observations obtained during the algorithm's progress (e.g., updating every fifth iteration to the GP hyperparameters), the dominated hypervolume fluctuates in response to changes in the maximum and minimum objective function values. Figure 15(a) shows the Pareto front as the algorithm progresses. Here, a solid colored line appears to the southwest of the previous ones, indicating that a new Pareto optimal set has emerged. In Figure 15(b), each plot depicts the trend of each normalized objective function value as the algorithm progresses. The numbers in parentheses near the red dots in Figures 15(a) and 15(b) denote the iteration numbers at that point. Figure 15(c) indicates that the dominated hypervolume remained unchanged through Iterations 15–26 and 27–100. Although the termination criterion was satisfied at Iteration 19, we continued the algorithm until Iteration 100, to enhance performance.

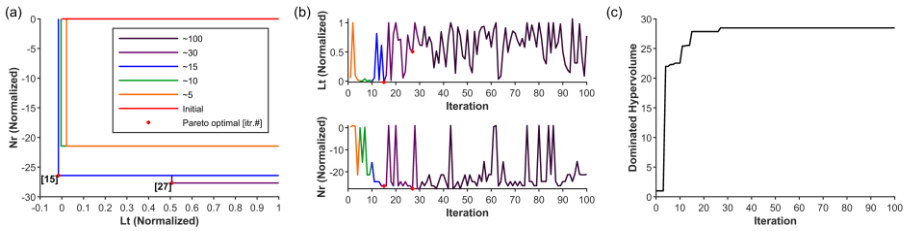

Figure 15 Multi-objective Bayesian optimization results for the Base Case over 100 iterations: (a) advance of the Pareto front as the iteration number increases, (b) the normalized objective function values (top: Lt, down: Nr) along the iterations, and (c) the dominated hypervolume along the iterations.

The Pareto front for the Base Case, including 18 initial observations and 100 new points, is obtained. The objective function values Lt and Pr (= 20 hours / Nr) at the optimized initial observations were 338.3 tons and 3 minutes, and the values at Iterations 15 and 27 were 338.1 and 344.3 tons, and 12.7 and 15.1 minutes, respectively. At Iteration 15, both objective function values were lower than their values at Iteration 27 and were improved relative to the initial observations. Although Pareto front saturation does not ensure global optimality (because the Pareto front can still be improved if the iterations continue) we decided to terminate the algorithm at the 100th iteration for the following reasons: As shown in Figure 15(c), no significant improvement was observed in the dominated hypervolume after Iteration 15. Nevertheless, the search for a new area for each objective function was adequately implemented during the iterations, as shown in Figure 15(b). Although the Pareto optimal sets were obtained only two at Iterations 15 and 27, the results showed that prolonging the replenishment period increased the reactant consumption. Furthermore, the maximum value of the expected improvement was sufficiently small (below 0.4) after the 34th iteration. Consequently, we concluded that the Pareto front became saturated after 27 iterations, and we applied the same stopping criteria to the Continuous and Buffer Cases without further iteration. Because the number of objective variable combinations for the two proposed cases was ~61–75 times higher than that of the Base Case, we concluded that a factor of 25% as the stopping criterion was sufficient to include new improvements in the vicinity of the solution after algorithm termination (e.g., Iteration 27 in the Base Case).

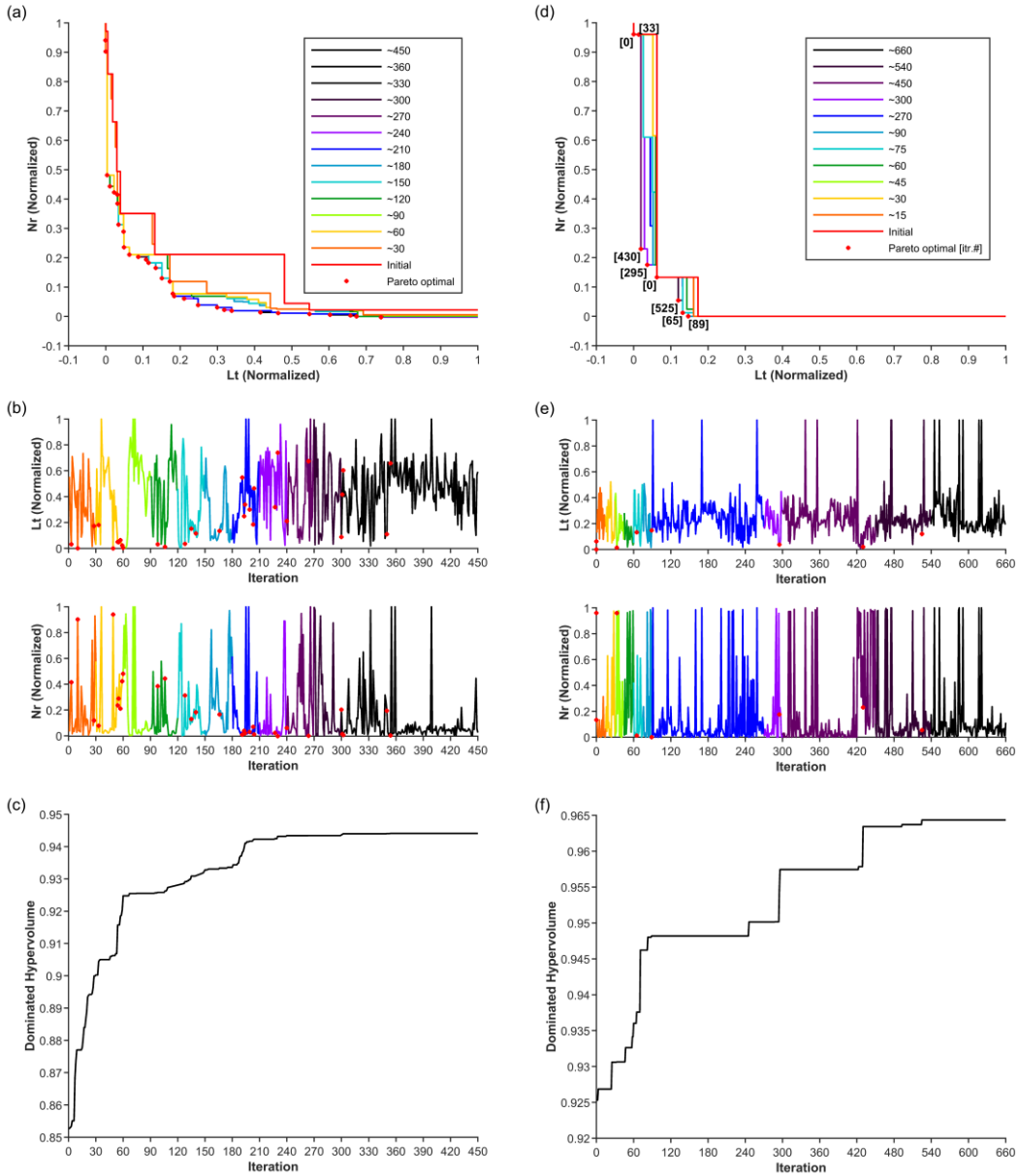

Figure 16 Multi-objective Bayesian optimization results for the Continuous Case (left) and Buffer Case (right).

Figure 16 shows the optimization results for the two proposed cases, similar to the Base Case results shown in Figure 15. The iterations shown in Figure 16(a) are [49, 10, 60, 106, 59, 3, 98, 128, 55, 54, 57, 300, 350, 140, 166, 135, 28, 33, 203, 240, 193, 199, 227, 194, 301, 204, 191, 302, 354, 264, 230] from lowest to highest on the x-axis. The iteration number "[0]" in Figure 16(d) indicates the initial observation point. The Pareto front for the Continuous Case [shown in Figure 16(a)] was smoother than the others, and the number of Pareto optimal sets was highest. This was because the optimization variable of the continuous flow Fc was discretized more finely than the others. For the same reason, the Pareto optimal sets for the Base and Buffer Cases formed two and three groups, respectively. However, it is possible that the two objective functions were not always in a trade-off relationship: the Pareto fronts for the Continuous Case and Buffer Case were discontinuous between normalized Nr values larger than 0.5 and 0.23, respectively, and the remaining values, as shown in Figure 16(a) and (d); meanwhile, the search for a new area for each objective function was sufficiently implemented, as shown in Figure 16(b) and 16(e). In fact, a long replenishment period requires a large replenishment quantity; however, the liquid level criterion of the second reactor need only be satisfied when the overall CO_2 removal efficiency exceeds 90% during operation. As shown in Figures 16(c) and 16(f), the dominated hypervolume became stagnant shortly after the algorithm started; hence, a factor of 0.25% was adopted in the stopping criterion, to prevent the algorithm from terminating prematurely. Furthermore, the algorithm continued for ~100 iterations after the final improvement to determine whether the algorithm is adequately implemented.

Table 16 Summary of multi-objective Bayesian optimization for the three operation recipe cases

	Base Case	**Continuous Case**	**Buffer Case**
# of initial observation	5	40	48
# of initial constraint violations	13	86	42
Total # of combinations	1,920	117,120	143,360
Lt / Pr Max (ton / min)	344.3 / 15.1	360.1 / 180.6	353.3 / 36.1
Lt / Pr Min (ton / min)	338.1 / 12.7	338.2 / 3.1	340.7 / 5.7
		⋮	⋮
Optimal results (ton / min [itr.#])	338.1 / 12.7 [15] **344.3 / 15.1 [27]**	342.2 / 16.3 [166] **345.6 / 51.6 [193]** 356.1 / 120.4 [302]	342.3 / 15.9 [430] **346.0 / 20.8 [0]** 352.0 / 33.9 [65]
		⋮	⋮
Product quality	~100 wt%	~97.5 wt%	~97.8 wt%
		⋮	⋮
Optimal input sets	[0.75 0.80 0.65] [0.73 0.79 0.74]	[0.72 0.75 0.65 0.34] [0.71 0.75 0.66 0.53] [0.71 0.77 0.71 0.59]	[0.74 0.80 0.79 0.66 0.68] [0.72 0.80 0.79 0.72 0.72] [0.66 0.80 0.74 0.75 0.69]
		⋮	⋮

Table 16 summarizes the optimization results for the three operation recipe cases. The total number of optimization variable combinations for the Buffer Case was highest; however, the sum of the numbers of initial observations and constraint violations for the Continuous Case exceeded the others, because the optimization variable Fc was discretized more finely than the others. The maximum values of Lt and Pr for the two proposed cases exceeded those of the Base Case, though the minimum values of Lt did not improve. In addition, the product qualities—that is, the boldfaced values under "Optimal results" in Table 6—for the two proposed cases were reduced compared to the Base Case, because the loss of the reactant increased after the additional sequences (i.e., the continuous flow Fc in the Continuous Case and Steps 1 and 2 in the Buffer Case). Nevertheless, the two proposed cases had the advantage in that the values of Pr were ~3.4 and ~1.4 times larger, respectively, compared to Iteration 27 of the Base Case. The values of Lt were decreased despite the increases in Pr at the 166th (Continuous Case) and 430th (Buffer Case) iteration.

In Table 16, the "Optimal input sets" refer to the input set that produced the "Optimal results." In the Base Case, a high liquid level fraction (v_2) of the first reactor during the operation was favorable to both Lt and Pr, and a higher replenishment quantity increased both Lt and Pr.

The higher Lt and Pr values for the Continuous Case were generated by the increased difference between v_1 and v_2, indicating a larger replenishment quantity for the higher continuous flow (v_4). In the Continuous Case, the highest Pr was 180.6 minutes, ~12 times larger than the results for Iteration 27 of the Base Case; the corresponding increase in Lt was ~4.6%.

The optimization results of the Buffer Case show that a higher buffer flow (v_2) to the first reactor is preferred, regardless of the other variables; furthermore, higher Lt and Pr values were produced by the larger difference between v_1 and v_3, indicating a higher replenishment quantity, as seen for the Continuous Case. In the Buffer Case, the product quality (i.e., the $CaCO_3$ content of the product) exceeded that of the Continuous Case, and both Lt and Pr were improved compared to the Base Case. However, these improvements were not significant. Nevertheless, the maximal Pr was ~2.4 times higher than the result for Iteration 27 of the Base Case, with a corresponding increase of ~2.6% in Lt.

Overall, a high liquid level in the second reactor is necessary to increase the replenishment quantity whilst maintaining an overall CO_2 removal efficiency exceeding 90%. However, a higher liquid level in the second reactor increases Lt. Thus, a trade-off relationship seems to arise between Lt and Pr, in which Pr increases as Lt increases. Consequently, because the Base Case recipe has a poor improvement potential, the two proposed operation recipes could, by extending the operational boundaries, help to prolong Pr and preserve Lt whilst satisfying the constraints.

4.5 Summary

The final objective of this study was to determine the optimal operation recipe that minimized the quantity of reactant used whilst maintaining an overall CO_2 removal efficiency exceeding 90% during operation. To ensure that the operational constraints were satisfied during operation, the process model was simulated dynamically, and all dynamic simulations were run for 20 hours

to reach the steady state. However, a long dynamic simulation time was required, and the reactant replenishment sequence in the semi-continuous process also required numerous iteration steps to converge the nonlinear solver. It took ~1–2 hours in real time to simulate one dynamic simulation run. To solve this problem, we adopted the Bayesian optimization algorithm—a powerful optimization tool for minimizing the number of expensive function evaluations—to optimize the operation recipe for the aqueous MC process; the ACM model was used as a black-box function in this algorithm.

The Base Case (Case 1) operation recipe—the sequence used in actual pilot-plant operations—has poor improvement potential, owing to its simplicity; hence, we proposed two new operation recipes: a sequence including both a continuous and discrete flow (Case 2; the Continuous Case) and one involving additional reactant replenishment (Case 3; the Buffer Case). Cases 1–3 featured 3, 4, and 5 optimization variables and 1,920; 117,120; and 143,360 combinations, respectively. Subsequently, by linking MATLAB to ACM, the multi-objective Bayesian optimization was implemented to minimize the quantity of reactant used (Lt) and to maximize the replenishment period (Pr).

A saturated Pareto front is obtained for Cases 1–3 after 100, 450, and 660 iterations, respectively. For all cases, Pr increased when Lt increased, which indicates a trade-off relationship. A higher liquid level of the second reactor was found favorable for increasing the replenishment quantity, though this also increased Lt. Compared to the Pareto optimal results for Iteration 27 of the Base Case, the highest Pr values for the Continuous and Buffer Cases were increased by factors of ~12 and ~2.4, respectively, corresponding increases of ~4.6% and

2.6%, respectively, were observed in Lt. However, the product quality for Cases 2 and 3 was lower than that of the Base Case; expressed otherwise, the reactant loss increased because the product was removed along with the supplementary reactant, because of the Fc and buffer flow, respectively. Consequently, the Base Case achieved the highest product quality, though it had a poor improvement potential. Thus, the operation recipes of the Continuous Case and Buffer Case may help to prolong Pr and preserve Lt whilst maintaining an overall CO_2 removal efficiency exceeding 90% during operations, by extending the operational boundaries.

Finally, we anticipate that the methodology used to optimize the operation recipe could be applied to cases in which the feed rates of the upstream flue gas are irregular, by varying the continuous flow Fc in the Continuous Case. In particular, because replenishment in the Base and Buffer Cases is conducted only when the reactants are completely consumed, the optimal operation recipe can be applied to those conditions without alteration within a similar process capacity. Although we obtained the discrete Pareto front, a more accurate Pareto front can be obtained by discretizing the set of optimization variables more finely or increasing the factors of the stopping criterion, provided the available computational resources are sufficient to tackle these evaluations. In addition, a specific set of optimal operation recipes can be obtained using the operation recipes proposed in this study, by considering the desired product quality, the price of the reactant solution, and the operating costs relevant to replenishment (e.g., the pump electricity, labor, and maintenance costs).

Chapter 5 Concluding remarks

In this thesis, process intensification is implemented with a lab-scale or pilot-scale experiment for improving the feasibility of eco-friendly chemical processes. First, the economic feasibility study on the intensified biodiesel production process is implemented to increase the profitability of the biodiesel production process by reducing the process units, enhancing biodiesel quality, and reducing the raw material cost. Comparative studies, including economic analysis, sensitivity analysis, product quality test, and side-effect consideration, are conducted between the conventional biodiesel production process, the SSTPH process with Cu catalyst, and the SSTPH with Pd/Al_2O_3 catalyst. The results show that the SSTPH with Pd/Al_2O_3 catalyst is the most economically feasible than the others in that it has the highest conversion to C18:1 from C18:2 and C18:3, the lowest CAPEX and OPEX owing to the mild reaction condition, and the lowest the break-even biodiesel price.

Secondly, the modeling and validation of the semi-continuous carbonation process are implemented to estimate the overall CO_2 removal efficiency during the operation and when the reaction ends. Lastly, developed process models can be applied to optimization algorithms to ensure operational feasibility and to obtain the optimal operation recipes. The constraint function, which is maintaining the overall CO_2 removal efficiency exceeding 90% during the operation, is included in the black-box model and the objective functions are the amount of reactant used and the number of replenishment. Bayesian optimization is a powerful tool for simultaneously optimizing hyperparameters whilst minimizing the number of expensive function evaluations required.

The reactor model, which has high non-linearity or is built on commercial software, can be used as a black-box function in Bayesian optimization algorithm. The multi-objective optimization of the operation recipes was successfully implemented, and the obtained Pareto front of proposed operation recipes outperform the basic operation recipe.

The proposed framework in this thesis for improving the feasibility of eco-friendly chemical processes, including the process intensification, modeling, economic analysis and optimization, can be illustrated as shown in Figure 17.

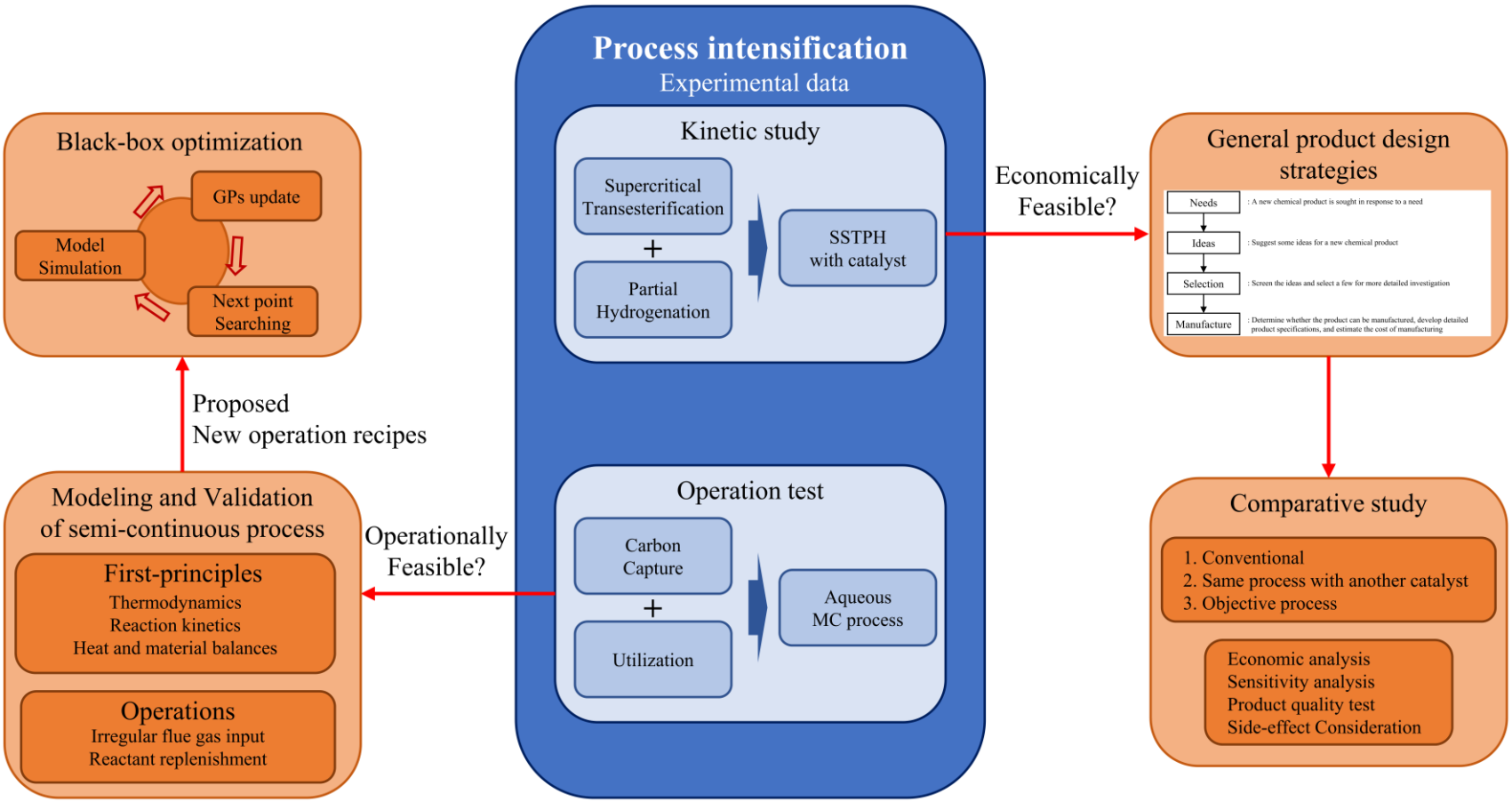

Figure 17 Schematic diagram of process intensification with feasibility study.

References

[1] Lee, D., Choi, J., Lee, Y. W., and Lee, J. M. (2021). Design and economic analysis of biodiesel production process of simultaneous supercritical transesterification and partial hydrogenation using soybean oil with Pd/Al2O3 catalyst. *Chemical Engineering Research and Design*.

[2] Lee, D., Na, J., Park, D., and Lee, J. M. (2021). Bayesian Optimization of Semicontinuous Carbonation Process Operation Recipe. *Industrial & Engineering Chemistry Research*.

[3] Shin, H. Y., Ryu, J. H., Bae, S. Y., and Kim, Y. C. (2013). "Biodiesel production from highly unsaturated feedstock via simultaneous transesterification and partial hydrogenation in supercritical methanol." *The Journal of Supercritical Fluids*, 82, 251-255.

[4] Lee, H. S., Seo, H., Kim, D., and Lee, Y. W. (2020). "One-pot supercritical transesterification and partial hydrogenation of soybean oil in the presence of Pd/Al2O3 or Cu or Ni catalyst without H2." *The Journal of Supercritical Fluids*, 156, 104683.

[5] Cussler, E. L. and Moggridge, G. D. (2011). *Chemical product design*., 2nd ed., New York: Cambridge University Press.

[6] Zhang, Y., Dube, M. A., McLean, D. D. L., and Kates, M. (2003). "Biodiesel production from waste cooking oil: 1. Process design and technological assessment." *Bioresource technology*, 89(1), 1-16.

[7] He, H., Sun, S., Wang, T., and Zhu, S. (2007). "Transesterification kinetics of soybean oil for production of biodiesel in supercritical methanol." *Journal of the American Oil Chemists' Society*, 84(4), 399-404.

[8] West, A. H., Posarac, D., and Ellis, N. (2008). "Assessment of four biodiesel production processes using HYSYS. Plant." *Bioresource Technology*, 99(14), 6587-6601.

[9] Lim, Y., Lee, H. S., Lee, Y. W., and Han, C. (2009). "Design and economic analysis of the process for biodiesel fuel production from transesterificated rapeseed oil using supercritical methanol." *Industrial & Engineering Chemistry Research*, 48(11), 5370-5378.

[10] Lee, S., Posarac, D., and Ellis, N. (2011). "Process simulation and economic analysis of biodiesel production processes using fresh and waste vegetable oil and supercritical methanol." *Chemical Engineering Research and Design*, 89(12), 2626-2642.

[11] Aboelazayem, O., Gadalla, M., Alhajri, I., and Saha, B. (2021). "Advanced process integration for supercritical production of biodiesel: Residual waste heat recovery via organic Rankine cycle (ORC)." *Renewable Energy*, 164, 433-443.

[12] Farobie, O. and Matsumura, Y. (2015). "Biodiesel production in supercritical methanol using a novel spiral reactor." *Procedia Environmental Sciences*, 28, 204-213.

[13] Trentin, C. M., Lima, A. P., Alkimim, I. P., da Silva, C., de Castilhos, F., Mazutti, M. A., and Oliveira, J. V. (2011). "Continuous catalyst-free production of fatty acid ethyl esters from soybean oil in microtube reactor using supercritical carbon dioxide as co-solvent." *The Journal of Supercritical Fluids*, 56(3), 283-291.

[14] Muppaneni, T., Reddy, H. K., Patil, P. D., Dailey, P., Aday, C., and Deng, S. (2012). "Ethanolysis of camelina oil under supercritical condition with hexane as a co-solvent." *Applied Energy*, 94, 84-88.

[15] Da Silva, C., De Castilhos, F., Oliveira, J. V., and Cardozo Filho, L. (2010). "Continuous production of soybean biodiesel with compressed ethanol in a microtube reactor." *Fuel Processing Technology*, 91(10), 1274-1281.

[16] Muppaneni, T., Reddy, H. K., Ponnusamy, S., Patil, P. D., Sun, Y., Dailey, P., and Deng, S. (2013). "Optimization of biodiesel production from palm oil under supercritical ethanol conditions using hexane as co-solvent: A response surface methodology approach." *Fuel*, 107, 633-640.

[17] Ziyai, M. R., Mehrpooya, M., Aghbashlo, M., Omid, M., Alsagri, A. S., and Tabatabaei, M. (2019). "Techno-economic comparison of three biodiesel production scenarios enhanced by glycerol supercritical water reforming process." *International Journal of Hydrogen Energy*, 44(33), 17845-17862.

[18] Ortiz, F. J. G. and Kruse, A. (2020). "The use of process simulation in supercritical fluids applications." *Reaction Chemistry & Engineering*, 5(3), 424-451.

[19] Goodrum, J. W. (2002). "Volatility and boiling points of biodiesel from vegetable oils and tallow." *Biomass and Bioenergy*, 22(3), 205-211.

[20] Robinson, C.S. and E.R. Gilliland, "*Elements of Fractional Distillation*," 4th ed., McGraw-Hill, New York, pp. 347–350 (1950).

[21] Newman, A.A., 1968. *Glycerol*., CRC Press, Cleveland (Chapter 6).

[22] Van Kasteren, J. M. N., and Nisworo, A. P. (2007). "A process model to estimate the cost of industrial scale biodiesel production from waste cooking oil by supercritical transesterification." *Resources, Conservation and Recycling*, 50(4), 442-458.

[23] You, Y. D., Shie, J. L., Chang, C. Y., Huang, S. H., Pai, C. Y., Yu, Y. H., and Chang, C. H. (2008). "Economic cost analysis of biodiesel production: case in soybean oil." *Energy & Fuels*, 22(1), 182-189.

[24] Kelloway, A., Marvin, W. A., Schmidt, L. D., and Daoutidis, P. (2013). "Process design and supply chain optimization of supercritical biodiesel synthesis from waste cooking oils." *Chemical Engineering Research and Design*, 91(8), 1456-1466.

[25] Sakdasri, W., Sawangkeaw, R., and Ngamprasertsith, S. (2018). "Techno-economic analysis of biodiesel production from palm oil with supercritical methanol at a low molar ratio." *Energy*, 152, 144-153.

[26] Turton, R., Bailie, R. C., Whiting, W. B., and Shaeiwitz, J. A. (2008). *Analysis, synthesis and design of chemical processes*., Pearson Education.

[27] Seider, W. D., Seader, J. D., Lewin, D. R., and Widagdo, S. (2009). *Product and process design principles* 3rd. edition.

[28] Macrotrends LLC, 2010, Soybean Oil Prices - 45 year Historical Chart. Available at : https://www.macrotrends.net/2538/soybean-oil-prices-historical-chart-data

[29] Methanol institute, Methanol price and supply/demand (United States Gulf Coast). Available at : https://www.methanol.org/methanol-price-supply-demand/

[30] NESTE wolrdwide, biodiesel prices (FAME). Available at : https://www.neste.com/investors/market-data/biodiesel-prices-sme-fame

[31] Alibaba Group, Glycerol market price. Available online at : https://www.alibaba.com/product-detail/Industrial-Glycerin-95-glycerol-prices_1072445803.html?spm=a2700.pc_countrysearch.main07.127.1d0b533bCi5S0F (Accessed December 06, 2020)

[32] Sigma-Aldrich, Palladium on alumina price. Available at : https://www.sigmaaldrich.com/catalog/product/aldrich/205710?lang=en&region=US

[33] Sigma-Aldrich, Copper price. Available at : https://www.sigmaaldrich.com/catalog/product/aldrich/357456?lang=en&region=US&cm_sp=Insite-_-caSrpResults_srpRecs_srpModel_357456-_-srpRecs3-1

[34] Johannsen, K. and Rademacher, S. (1999). "Modelling the kinetics of calcium hydroxide dissolution in water." *Acta hydrochimica et hydrobiologica*, 27(2), 72-78.

[35] Na, J., Park, S., Bak, J. H., Kim, M., Lee, D., Yoo, Y., ... and Lee, J. M. (2019). "Bayesian inference of aqueous mineral carbonation kinetics for carbon capture and utilization." *Industrial & Engineering Chemistry Research*, 58(19), 8246-8259.

[36] Zhang, D., Deen, N. G., and Kuipers, J. A. M. (2007). "Numerical modeling of hydrodynamics, mass transfer and chemical reaction in bubble Columns." *In 6th International Conference on Multiphase Flow*, ICMF 2007.

[37] Akita, K. and Yoshida, F. (1974). "Bubble size, interfacial area, and liquid-phase mass transfer coefficient in bubble columns." *Industrial & Engineering Chemistry Process Design and Development*, 13(1), 84-91.

[38] Lozhechnikova, A. (2011). *Determination of slurry's viscosity using case based reasoning approach.*

[39] Hikita, H. and Kikukawa, H. (1974). "Liquid-phase mixing in bubble columns: Effect of liquid properties." *The Chemical Engineering Journal*, 8(3), 191-197.

[40] Brauer, H. (1981). "Particle/fluid transport processes." *Prog. Chem. Eng.*, 19, 61-99.

[41] Westerterp, K. R., van Swaaij, W. P., Beenackers, A. A. C. M., and Kramers, H. (1984). *Chemical reactor design and operation*.

[42] Weisenberger, S. and Schumpe, D. A. (1996). "Estimation of gas solubilities in salt solutions at temperatures from 273 K to 363 K." *AIChE Journal*, 42(1), 298-300.

[43] Versteeg, G. F. and Van Swaaij, W. P. (1988). "Solubility and diffusivity of acid gases (carbon dioxide, nitrous oxide) in aqueous alkanolamine solutions." *Journal of Chemical & Engineering Data*, 33(1), 29–34.

[44] Pohorecki, R. and Moniuk, W. (1988). "Kinetics of reaction between carbon dioxide and hydroxyl ions in aqueous electrolyte solutions." *Chemical engineering science*, 43(7), 1677-1684.

[45] Edwards, T. J., Maurer, G., Newman, J., and Prausnitz, J. M. (1978). "Vapor-liquid equilibria in multicomponent aqueous solutions of volatile weak electrolytes." *AIChE Journal*, 24(6), 966-976.

[46] Eigen, M. (1954). "Methods for investigation of ionic reactions in aqueous solutions with half-times as short as 10–9 sec. Application to neutralization and hydrolysis reactions." *Discussions of the Faraday Society*, 17, 194-205.

[47] Hikita, H., Asai, S., and Takatsuka, T. (1976). "Absorption of carbon dioxide into aqueous sodium hydroxide and sodium carbonate-bicarbonate solutions." *The Chemical Engineering Journal*, 11(2), 131-141.

[48] Tsonopoulos, C., Coulson, D. M., and Inman, L. B. (1976). "Ionization constants of water pollutants." *Journal of chemical and engineering data*, 21(2), 190-193.

[49] Danckwerts, P. V. (1966). "The absorption of carbon dioxide into solutions of alkalis and amines (with some notes on hydrogen sulfide and carbonyl sulfide)." *The Chemical Engineer*, 244-280.

[50] Plummer, L. N. and Busenberg, E. (1982). "The solubilities of calcite, aragonite and vaterite in CO2-H2O solutions between 0 and 90 C, and an evaluation of the aqueous model for the system CaCO3-CO2-H2O." *Geochimica et Cosmochimica Acta*, 46(6), 1011-1040.

[51] Velts, O., Uibu, M., Kallas, J., and Kuusik, R. "Waste oil shale ash as a novel source of calcium for precipitated calcium carbonate: Carbonation mechanism, modeling, and product characterization." *Journal of Hazardous Materials*. 2011, 195, 139–146.

[52] Yuan, T., Wang, J., and Li, Z. (2010). "Measurement and modelling of solubility for calcium sulfate dihydrate and calcium hydroxide in NaOH/KOH solutions." *Fluid phase equilibria*, 297(1), 129-137.

[53] Brochu, E., Cora, V. M., and De Freitas, N. (2010). "A tutorial on Bayesian optimization of expensive cost functions, with application to

active user modeling and hierarchical reinforcement learning." *arXiv preprint arXiv*:1012.2599.

[54] Svenson, J. and Santner, T. (2016). "Multiobjective optimization of expensive-to-evaluate deterministic computer simulator models." *Computational Statistics & Data Analysis*, 94, 250-264.

[55] Jones, D. R., Schonlau, M., and Welch, W. J. (1998). "Efficient global optimization of expensive black-box functions." *Journal of Global optimization*, 13(4), 455-492.

[56] Bect, J. and Vazquez, E. et. al. STK: a Small (Matlab/Octave) Toolbox for Kriging. Release 2.5.1. In. 2018.

Abstract in Korean (국문초록)

기후 변화로 인한 위험들을 완화하는 기술들은 학술 분야와 산업 모두에서 상당한 발전을 이루었다. 그러나 대부분의 진보된 기술들은 여전히 실험실 규모의 실험에서만 고려되고 있다. 더욱이, 공정 합성 과정에서의 공정 강화 개발은 초기 단계에 머물러있다. 새로운 공정 기술들을 친환경 공정에 적용하는 것을 촉진시키기 위해서는, 공정의 경제성 또는 운전 타당성을 고려해야 한다.

본 학위논문에서는 제한된 실험 조건 하에서 제안된, 강화된 친환경 공정의 시뮬레이션 기반 타당성 개선 방법론을 제시하였다. 이론적인 검증을 통한 공정 강화가 아닌 수많은 실험을 통해 제안되는 공정 강화의 방식에서 파생되는 타당성 검증에 대한 문제를 해결하고자, 공정 및 반응기의 모델을 구축하고 다양한 상황을 모사하는 디지털 트윈 기술을 구현하였다. 또한, 구축된 디지털 트윈 모델의 검증부터, 강화된 공정의 경제적 타당성 및 운전 타당성 검증 및 개선까지의 일련의 과정들을 포함하는 방법론을 제시하였다.

먼저, 바이오디젤 생산 공정과 탄소 포집 및 활용 공정과 같은 강화된 친환경 공정을 시뮬레이션하고, 해당 공정의 경제적 타당성 또는 운전 타당성을 개선하기 위해 비교 연구 및 최적화를 수행하였다. 경제적 타당성 검증 방법론을 적용한 한가지 예제로써, 공정 유닛을 줄이고, 바이오디젤 품질 향상 및 원재료 비용을

감소시킴으로써 바이오디젤 생산 공정의 수익성을 증가시키는 강화된 바이오디젤 생산 공정의 경제적 타당성 연구를 수행하였다. 운전 타당성 검증 방법론을 적용한 한가지 예제로써, 반연속식 탄산화 공정의 운전 중 전체 이산화탄소 제거 효율과 반응 종료 시기를 추정하기 위해 시뮬레이션 기반 모델링 및 구축된 모델의 검증을 수행하였다. 구축된 시뮬레이션 기반 모델을 이용하여, 반연속식 탄산화 공정의 운전 타당성을 확인하고 최적의 운전 레시피를 얻기 위해 최적화 알고리즘에 적용하였다. 효과적인 반연속식 탄산화 공정의 운영 타당성 개선을 위해 두개의 새로운 운전 레시피를 제시하였고, 베이지안 최적화 기법을 이용하여 최적화하였다.

결론적으로, 반응식 및 반응 계수 연구를 위한 실험실 규모의 실험 데이터를 활용하여 공정 모델을 구축하고, 경제성 분석, 민감도 분석, 비교 분석을 통해 새로 제안된 강화된 공정의 현업에의 적용 가능성을 검증하고 개선시키는 방법론을 제안하였다. 또한, 실제 현업에 적용되는 크기의 반응기를 가진 중간 규모의 실험 데이터를 활용하여 공정 모델을 구축하고 최적화하였다. 특히, 반연속식 공정의 새로운 운전 방식을 제안함과 동시에 구축된 디지털 트윈 모델에 블랙박스 (Black-box) 최적화 기법을 적용하여 제안된 반연속식 친환경 공정의 운전 타당성을 효과적으로 개선할 수 있었다.

본 학위논문에서는 목적에 따라 다른 두 가지의 실험 결과를 이용하여, 새롭게 제안된 강화된 친환경 공정의 경제적 또는 운전 타당성 검증 및 개선을 위한 방법론을 제시하였다.

주요어: 공정 강화, 바이오디젤 생산 공정, 탄소 포집 및 활용 공정, 블랙박스 반응기 모델, 베이지안 최적화.

학 번 : 2015-22820